Available online at www.sciencedirect.com

ScienceDirect

Underground Space 27 (2026) 1–23

www.keaipublishing.com/undsp

Research Paper

Combined active and passive support technology and its application for deformation control in large-section weakly cemented tunnel

Qing Ma [a,c], Wei Zhang [b,*], Xiaoli Liu [c], Weiqiang Xie [c], Ruosong Wang [d], Jinpeng Zhao [c]

[a] *Beijing Key Laboratory of Urban Underground Space Engineering, University of Science and Technology Beijing, Beijing 100083, China*
[b] *School of Architecture and Engineering, Liaocheng University, Liaocheng 252000, China*
[c] *State Key Laboratory of Hydroscience and Engineering, Tsinghua University, Beijing 100084, China*
[d] *Shandong Energy Xinwen Group Xinjulong CO. LTD., Shandong 294718, China*

Received 17 September 2024; received in revised form 24 September 2025; accepted 28 October 2025
Available online 8 January 2026

Abstract

The development of large cross-section tunnels is an inevitable trend driven by the intensification of coal mining activities and advancements in mining equipment technology. However, the disturbance stress exerted by adjacent caverns has a more pronounced impact on weakly cemented rock strata in the vicinity of neighboring tunnels. To mitigate deformation in weakly cemented tunnels, grouting and the installation of long anchor cables were employed to reinforce the self-supporting capacity of the surrounding rock, thereby establishing an active support layer. Additionally, U-shaped steel frames combined with the subsequent application of flexible filling materials were utilized to aid the surrounding rock in mobilizing its self-supporting capacity, which resulted in the formation of a passive support layer. A layered collaborative control methodology integrating both active and passive support mechanisms was developed and implemented in engineering practice. The findings demonstrate that the vertical stress was alleviated after cavern excavation and was predominantly transferred toward the adjacent tunnel, with the influence zone extending approximately 7 to 12 times the tunnel height. Conversely, the horizontal stress is primarily dispersed laterally, affecting a region approximately 3 to 6 times the tunnel width. Following the infilling of pebbles between the U-shaped steel frame and the adjacent rock mass, the maximum compressive stress experienced by the U-shaped steel frame decreased by 50%. Additionally, the spatial extent of the maximum axial force was reduced by 65%, whereas the stresses within the rock bolts and cable bolts increased by 30% and 40%, respectively. Grouting reinforcement contributed to bonding and compaction effects on the delamination and fracturing of the roof strata, with the grout predominantly distributed within a range of 1.5 to 5 m from the central region of the roof. The research outcomes presented in this paper can provide valuable reference for a large-section weakly cemented tunnel.

Keywords: Weakly cemented rock; Large cross-section caverns; Large deformation tunnel; Active-passive collaborative control; Grouting reinforcement

1 Introduction

At present, the coal resources in eastern China are gradually depleting, and the development scale in central China is approaching its limit (Feng et al., 2022; Ma et al., 2023; Meng et al., 2023). The western region has abundant coal resources, accounting for approximately 66% of China's total, and as of 2021, the remaining proven technical recoverable reserves of coal in this region were 162.288 Gt (Chen et al., 2022; Hu et al., 2023; Ru et al., 2023; Wang et al., 2019). Therefore, achieving efficient development of coal resources in the western region has become an important means of supporting China's energy industry and achieving the "dual carbon" goals as scheduled, and is of great significance for promoting high-quality economic development

* Corresponding author.
E-mail address: zhangw@lcu.edu.cn (W. Zhang).
Peer review under the responsibility of Tongji University

https://doi.org/10.1016/j.undsp.2025.10.007

in China and globally (Li et al., 2020; Ma et al., 2019, 2020; J. Zhao et al., 2022).

The coal-bearing strata in the western mining areas of China are primarily composed of the Cretaceous and Jurassic strata (Zhang et al., 2023; Zhao et al., 2019). These strata have a unique diagenetic age, environment, and sedimentary process, and the coal seam is primarily composed of weakly cemented rocks (Zhao et al., 2017). Unlike the Carboniferous and Permian rock formations commonly found in eastern China, the soft rocks in this region exhibit unique physical and mechanical properties. The rocks are relatively intact and possess a certain level of inherent strength under natural conditions. However, they are highly susceptible to disturbance, weathering, and disintegration upon exposure to water, often softening into mud. Most of the rocks are poorly lithified and primarily bonded by argillaceous cement (Chen et al., 2019; Le & Airey, 2023; Yang et al., 2019; Zhang & Gao, 2020) with rock quality index (RQD) of 14%–26%, uniaxial compressive strength of 5–15 MPa, and softening coefficient of 0.15–0.29 (Watanabe & Tanaka, 2023; Wu et al., 2023). The abovementioned parameters are significantly lower than those of typical soft rocks in other regions, resulting in poor self-stabilization capacity of the weakly cemented surrounding rock and a high susceptibility to large deformation. This disparity renders the theoretical knowledge and engineering experience accumulated during tunnel construction in eastern mining areas insufficient to fully address the demands of western projects, thereby posing new challenges for tunnel stability control in western regions (Tan et al., 2022; Zhang et al., 2022). In fact, weakly cemented rock is often encountered in tunnel engineering (Zhao et al., 2021). The findings of this study may also provide valuable insights into the stability control of tunnels constructed in weakly cemented rock strata.

With the continuous increase in mining intensity and mechanization of coal resources in the western region, the application of high mining height fully mechanized mining technology has become widespread (Yang et al., 2018; Miao et al., 2023). The tendency toward large-span and high sidewall caverns has resulted in a significant increase in the number of large cross-section caverns with an area of 20–25 m^2, with distance between adjacent caverns mostly within the range of 20–30 m, which can easily induce stress concentration (Ma et al. 2023; Zhang et al., 2024a, 2024b). The surrounding rock of weakly cemented tunnels exhibits complex characteristics such as continuous, large deformations, resulting in severe damage (J. Zhao et al., 2022; Zhao et al., 2024). The degree, scope, and frequency of catastrophic accidents such as support failure, roof collapse, and floor heave that occur in weakly cemented tunnels are greater than those in general soft rock tunnels. Repaired soft rock tunnels after excavation account for 65% of the total, increasing the support cost per unit of coal mining by more than 100% (Dai et al., 2025; Zhang et al., 2023). Regarding the failure mechanism of weakly cemented rock, Mineo and Pappalardo (2019) proposed that such rock enters the plastic state rapidly and over a wide range, with the plastic zone tending to extend beyond the support range, thereby hindering the full anchoring effect of rock bolts. Liu et al. (2019) found that the shear dilation effect has a relatively low impact on the range and stress response of the plastic zone in weakly cemented surrounding rock, but a greater impact on its damage rate and displacement. Swan and Li (2023) studied the characteristics of creep rate and failure modes of weakly cemented soft rocks and accordingly proposed a creep model to reflect the properties. Mezza et al. (2022) conducted a progressive failure study on weakly cemented rocks and found that the volume expansion deformation process of rocks is relatively long, exhibiting local stage plastic flow characteristics and delay effects during failure. Mineo et al. (2021) established mechanical models for different tunnel layouts in weakly cemented strata and obtained the evolution characteristics of tunnel failure under different rock stiffness conditions. Cao et al. (2021) and Bai et al. (2021) respectively proposed the theory of high prestressed support and differential support methods, with both theories using the combined support technology of high prestressed anchor rods and anchor cables to control the deformation of the surrounding rock. Cai et al. (2020), Han et al. (2022), and Vazaios et al. (2019) developed high prestressed anchor rods with increased resistance to large deformation, long and short anchor cable hierarchical control technology, and full-length prestressed support systems based on the matching characteristics between anchor components. Sivakumar et al. (2021) proposed the rigid flexible layer truss coupling support technology for jointed soft rock under high stress and strong expansion conditions. Xie et al. (2022) proposed a multilevel coupled support system with high-strength anchor cables and compressible annular supports as the core for stress expansion type geological soft rock. C. Zhang et al. (2020) proposed a coupled support technology with constant resistance and large deformation anchor rods. X. Zhang et al. (2020) and Agheshlui et al. (2019) analyzed the mechanism by which grouting enhances the self-supporting capacity of soft rock and proposed a collaborative support method combining anchoring and grouting. After encountering water in the strata, Afrasiabian et al. (2022) studied the deformation law and proposed dynamic control technology for water swelling type soft rock.

The above research results have important guiding significance for engineering applications and provide a basis for further research into the stability control of weakly cemented rocks (Tao et al., 2023; Wei et al., 2023). As a complex geological object, weakly cemented rocks are easily affected by external environments, leading to diverse failure mechanisms. The corresponding control methods cannot rely solely on a single support technology but need to integrate multiple support methods for effective reinforcement (Hoang et al., 2020; X. Zhang et al., 2020). Considering the research on large deformation of surrounding rock caused by support structure failure of weakly

cemented tunnels in the mining area of Inner Mongolia, this paper analyzes the expansion law of the plastic zone of weakly cemented surrounding rock and mechanism of tunnel instability. Based on the support method combining anchor rod, anchor cable, anchor net, and surface spray grouting, a layered active–passive combined control method is proposed, incorporating U25 steel frame, flexible material filling behind the frame, and grouting. During the one-year monitoring process, the above methods effectively controlled the deformation of the surrounding rock, providing a reference for the deformation control of weakly cemented tunnels in western mining areas.

2 Project profile

2.1 Geological conditions

The weakly cemented tunnel under investigation is situated in the northern region of the Ordos Plateau, China, specifically along the northern boundary of the Dongsheng Coalfield. The geological formation exhibits a monoclinic structure inclined toward the southwest, characterized by a dip angle of less than 5°. The area is characterized by locally developed broad and subtle undulations, with an absence of large-scale folding or faulting structures and no evidence of magmatic activity. As illustrated in Fig. 1, the topography of the study area exhibits a gradient descending from north to south, with elevations ranging between 1380 and 1480 m. The region is predominantly characterized by the presence of valleys and low to medium elevation mountainous landforms, which have undergone significant erosional processes.

The coal strata associated with the weakly cemented tunnel correspond to the Upper Triassic Yan'an Formation (T3y), which serves as the sedimentary basement for the Jurassic coal accumulation basin and its coal deposits. The coal seam exhibits a complex structural configuration characterized by well-developed joint systems. Although the spatial position of the coal seam remains relatively consistent, its thickness varies considerably, making it an unstable coal seam. Consequently, the seam is only locally amenable to mining operations. Figure 2 illustrates that the predominant lithologies in the tunnel roof and floor are fine sandstone, mudstone, and sandstone. The regional stratigraphic framework encompasses the Jurassic, Cretaceous, Neogene, Quaternary Pleistocene, and Holocene periods. The northern margin of the Dongsheng Coalfield has been significantly affected by Cenozoic tectonic activities, resulting in the erosion and incision of the upper strata by tributary systems. The stratigraphic sequence exhibits a chronological progression from older to younger formations, including the Upper Triassic Yanchang Formation (T3y), Middle Jurassic Yan'an Formation (J1-2y), Middle Jurassic Zhiluo Formation (J2z), Middle Jurassic Anding Formation (J2a), Lower Cretaceous Zhidan Formation (K1zh), and Quaternary deposits (Q).

2.2 Distribution characteristics of weakly cemented tunnels

The 2-1 weakly cemented tunnel is situated within the No. 2 coal seam, which has a burial depth ranging from 400 to 420 m. The thickness of the No. 2 coal seam varies between 0.9 and 4.4 m, with an average thickness of approximately 2 m. The seam exhibits a dip angle between 1° and 3°, averaging around 1.5°. As illustrated in Fig. 3, the tunnels designated as 3-1, 3-2, 3-3, and 3-4, situated beneath the 2-1 tunnel, are located within the #3 coal seam. The thickness of the #3 coal seam varies between 2.9 and 6.9 m, with a mean thickness of 5.3 m. The seam exhibits a dip angle ranging from 2° to 4°, averaging 2.7°. Both the #2 and #3 coal seams employ strike longwall retreat mining with comprehensive mechanization for their working faces and utilize natural roof collapse to manage the overlying strata within the goaf.

2.3 Physical and mechanical properties of rocks

As illustrated in Fig. 4, samples were collected at the excavation face located 60 m from the entrance of the 2-1 tunnel. After sampling, the coal and rocks were processed separately into a 100 mm × Φ50 mm cylindrical specimen and 25 mm × Φ50 mm disk specimen, respectively. Cylindrical samples were subjected to uniaxial and triaxial compression testing, whereas circular samples were evaluated

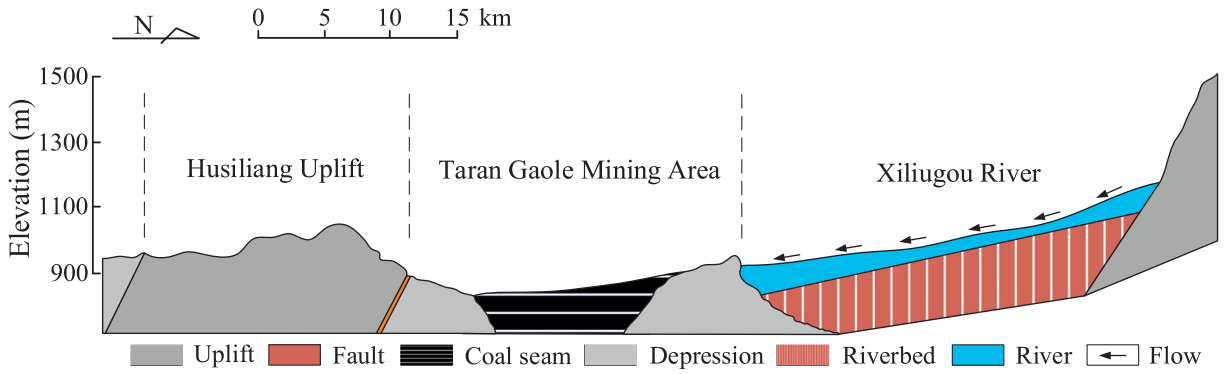

Fig. 1. Schematic of geological conditions in the mining area.

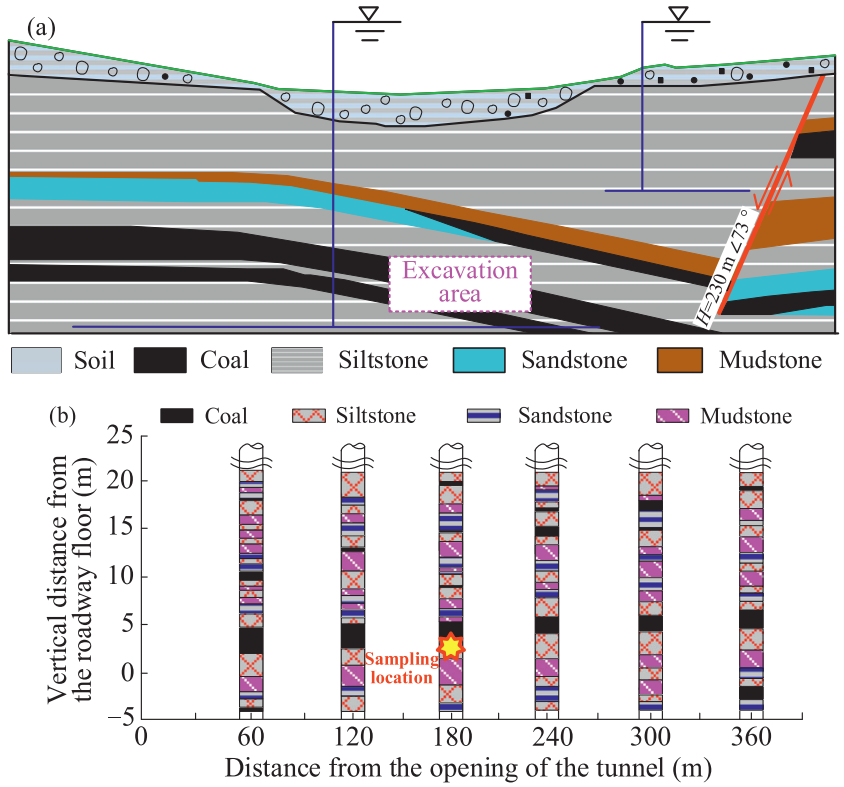

Fig. 2. Schematic of geological conditions for tunnel engineering. (a) Geological conditions along the tunnel axis, and (b) rock drilling sampling bar chart.

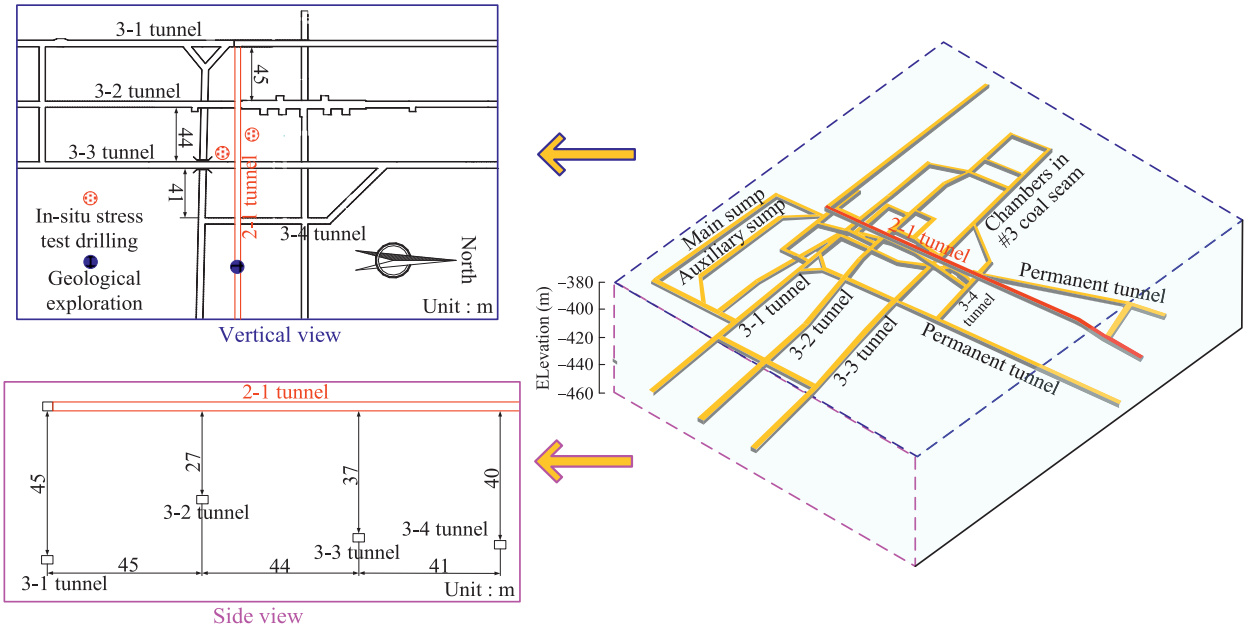

Fig. 3. Schematic of weakly cemented tunnel layout.

using Brazilian disc splitting tests. The results obtained from these experiments are compiled in Table 1.

As illustrated in Fig. 5, microscopic and scanning electron microscopy analyses were performed on coal, siltstone, sandstone, and mudstone samples. The physical composition results for mudstone, siltstone, and sandstone are presented in Fig. 6. The mineralogical composition of siltstone consists of quartz (30%–45%), biotite (10%–25%), plagioclase (0–15%), chlorite (5%–15%), and interstitial materials (25%–40%). Mudstone is primarily composed of quartz (15%–25%), albite (20%–30%), illite (30%–55%), and chlorite (0–15%). Sandstone comprises quartz

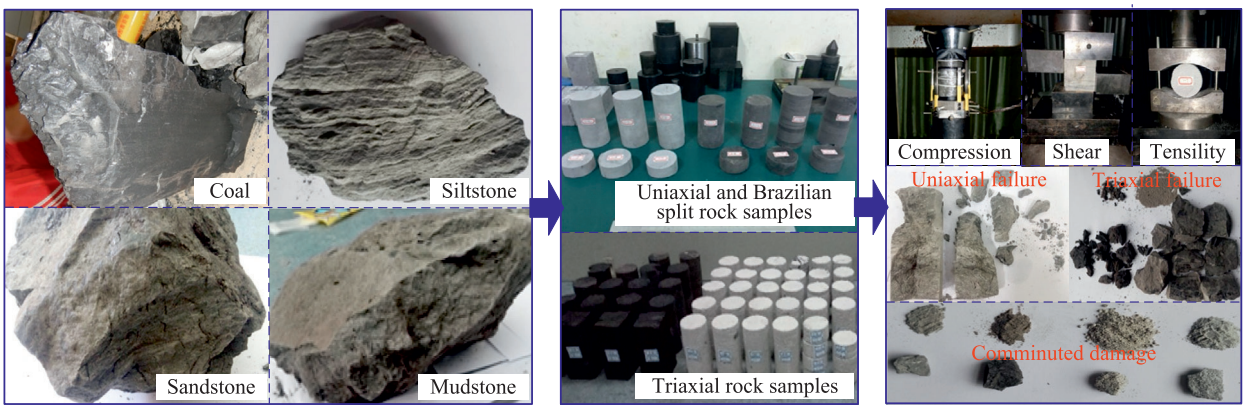

Fig. 4. Testing of mechanical properties of weakly cemented rocks.

Table 1
Physico-mechanical properties of weakly cemented rock.

Rock type	Density ($g \cdot cm^{-3}$)	Compressive strength (MPa)	Tensile strength (MPa)	Cohesion (MPa)	Elastic modulus (GPa)
Coal	2.33	14.77	4.02	3.21	2.25
Mudstone	2.19	10.23	3.58	2.54	1.89
Siltstone	2.41	15.45	4.28	3.52	2.44
Sandstone	2.08	12.23	3.22	2.59	2.01

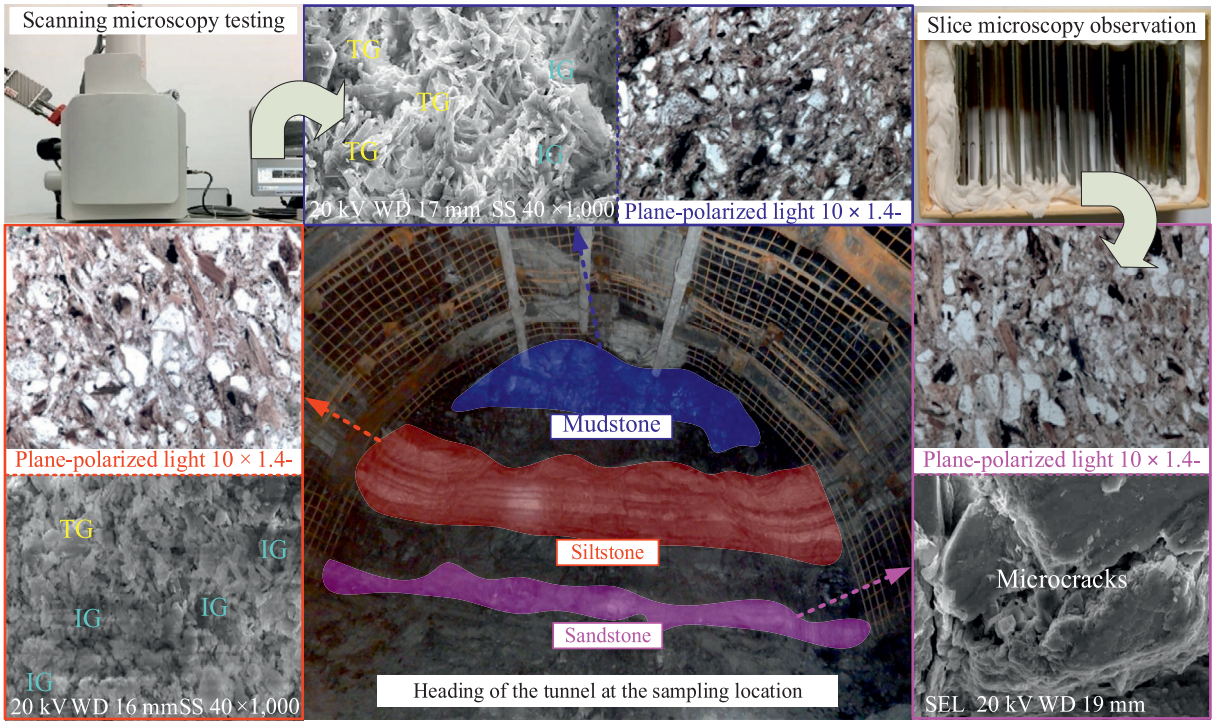

Fig. 5. Microscopic analysis of sampled rocks.

(20%–25%), albite (15%–30%), illite (20%–35%), and chlorite (15%–25%). Notably, the clay minerals present within the rock fragments and interstitial materials predominantly include montmorillonite, illite, and montmorillonite-illite interlayers. Based on these characteristics, siltstone is categorized as a weakly expansive soft rock, whereas mudstone and sandstone are classified as expansive soft rocks.

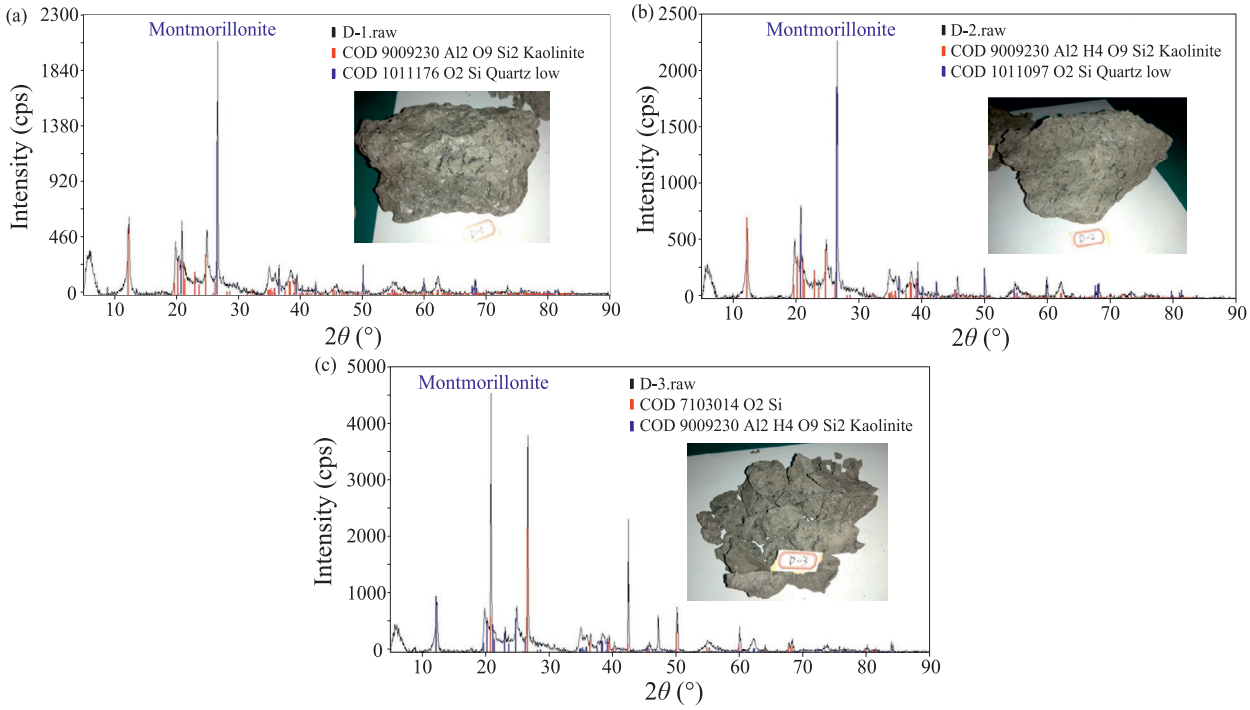

Fig. 6. Analysis results of physical properties and components of sampled rocks. (a) Mudstone, (b) siltstone, and (c) sandstone.

Table 2
Results of ground stress test.

Borehole	σ_v (MPa)	σ_H (MPa)	σ_h (MPa)	Direction of geostress
#1	10.24	15.21	4.58	N58.4°E
#2	10.19	14.99	5.13	N47.3°E

Note: σ_v is the vertical stress, σ_H is the maximum horizontal principal stress, and σ_h is the minimum horizontal principal stress.

The ground stress was evaluated using the stress relief method through core drilling, with the results presented in Table 2. Specifically, borehole #1 is situated on the left side of the 2-1 tunnel at a distance of 170 m from the tunnel entrance, and has an approximate depth of 13.4 m. Borehole #2 is positioned on the right side of the 2-1 tunnel, 190 m from the entrance, with an approximate depth of 15.8 m.

The lateral pressure coefficient for the 2-1 tunnel was quantified as 1.5. The predominant orientation of the maximum horizontal principal stress is toward the northeast, forming an angle of 53° relative to the longitudinal axis of the 2-1 tunnel.

3 Deformation characteristics of weakly cemented tunnel

The excavation of the 2-1 tunnel employed a support system comprising a combination of anchor rods and cables. As illustrated in Fig. 7, the roof support system comprised anchor rods, cables, steel mesh, steel ladders, and shotcrete, while the sides were supported by anchor rods, steel mesh, steel ladder, and shotcrete. The size of the anchor cable is Φ21.6 mm × 7300 mm, with a spacing of 1200 mm × 1200 mm. The size of the anchor cable support plate is 300 mm × 300 mm × 12 mm. Anchor rod selection Φ (diameter) = 20 mm, and L (length) = 2200 mm for the left-handed high-strength threaded steel anchor rod without longitudinal reinforcement, with a spacing of 800 mm × 800 mm. The size of the anchor rod support plate is 150 mm × 150 mm × 10 mm. Each anchor rod is equipped with an MSK2360 anchoring agent. The size of the steel ladder is Φ = 12 mm, b (grid width) = 100 mm, and L = 4100 mm. The shotcrete possesses a compressive strength classification of C25 and is applied at a thickness of 150 mm.

Figure 8 illustrates the arrangement of the tunnel deformation monitoring section (A, B, C, D) in the 2-1 tunnel. During the excavation process, the 2-1 tunnel underwent significant roof subsidence, floor heaving, and deformation of the tunnel walls. To understand the deformation behavior of the 2-1 tunnel, four sections were selected for analysis: section A, which exhibited slight deformation, and sections B, C, and D, which experienced severe damage. Monitoring points were established at intervals of 75 m. Data collection commenced when excavation reached section A, with measurements recorded every two days over a period of 49 days. This data acquisition protocol was similarly applied to the other monitoring points. Surface deformation was assessed using the cross-point method, while the forces exerted on anchor rods and cables were measured using force gauges. The monitoring scope encompassed roof subsidence, floor heave, lateral

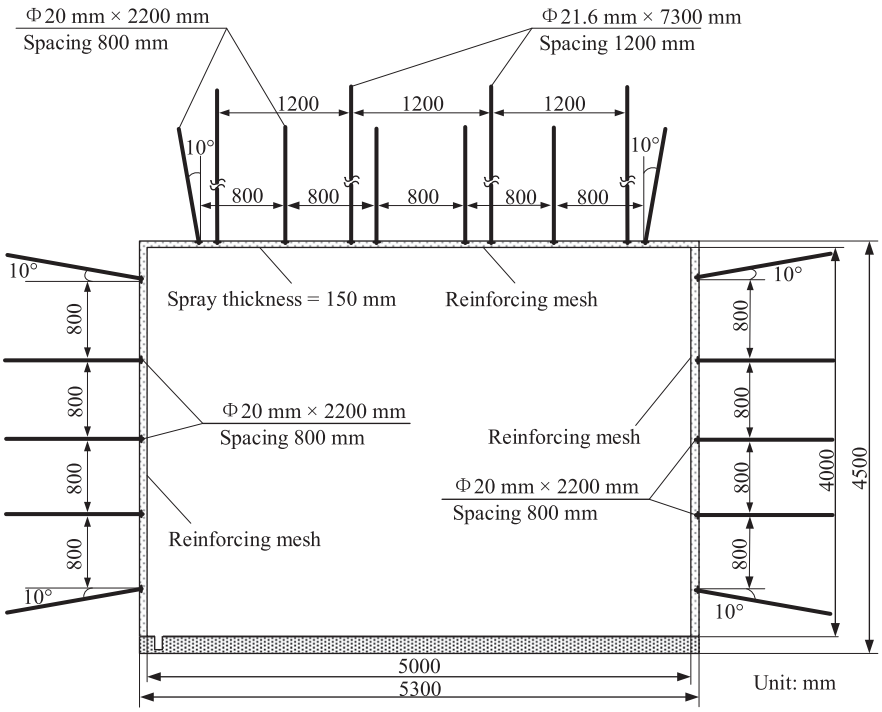

Fig. 7. Support scheme of weakly cemented tunnel.

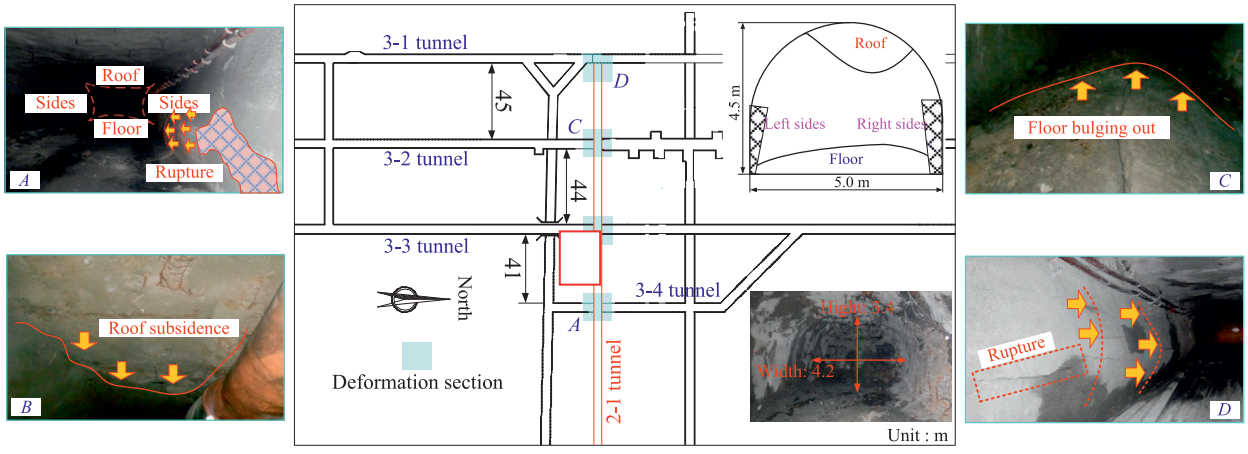

Fig. 8. Schematic of weakly cemented tunnel failure.

movements of the tunnel walls, and the stress states of the anchor rods and cables.

The cumulative deformation of the tunnel roof at measurement sections *B*, *C*, and *D* reached 616, 588, and 674 mm, respectively, over a monitoring period of 49 days, as illustrated in Fig. 9. Within the initial 28 days of monitoring, these points exhibited cumulative deformations of 474, 517, and 489 mm, respectively. During this interval, the tunnel roof experienced a notably rapid deformation, with a maximum settlement rate of approximately 44.9 mm per day. Specifically, between the 14th and 28th days, the cumulative deformation at points *B*, *C*, and *D* was 242, 224, and 273 mm, respectively. Subsequently, from the 35th to the 49th day, the deformation rate of the tunnel surface decelerated, with approximately 15.1 mm per day as the highest observed rate. In summary, the deformation profile of tunnel 2-1 can be ranked according to location as follows: roof (642 mm) > floor (457 mm) > right side (255 mm) > left side (158 mm).

An examination of the load-time curve for the support structure depicted in Fig. 10 reveals that the load borne by the anchor rods and cables diminishes with extended support duration. This reduction is more pronounced during the initial phase and becomes progressively less significant over time. Furthermore, analysis of the load-time curves for sections *B*, *C*, and *D* indicates a gradual increase in load from day 1 to day 21, with the rate of increase decelerating over this period. The load on anchor rods

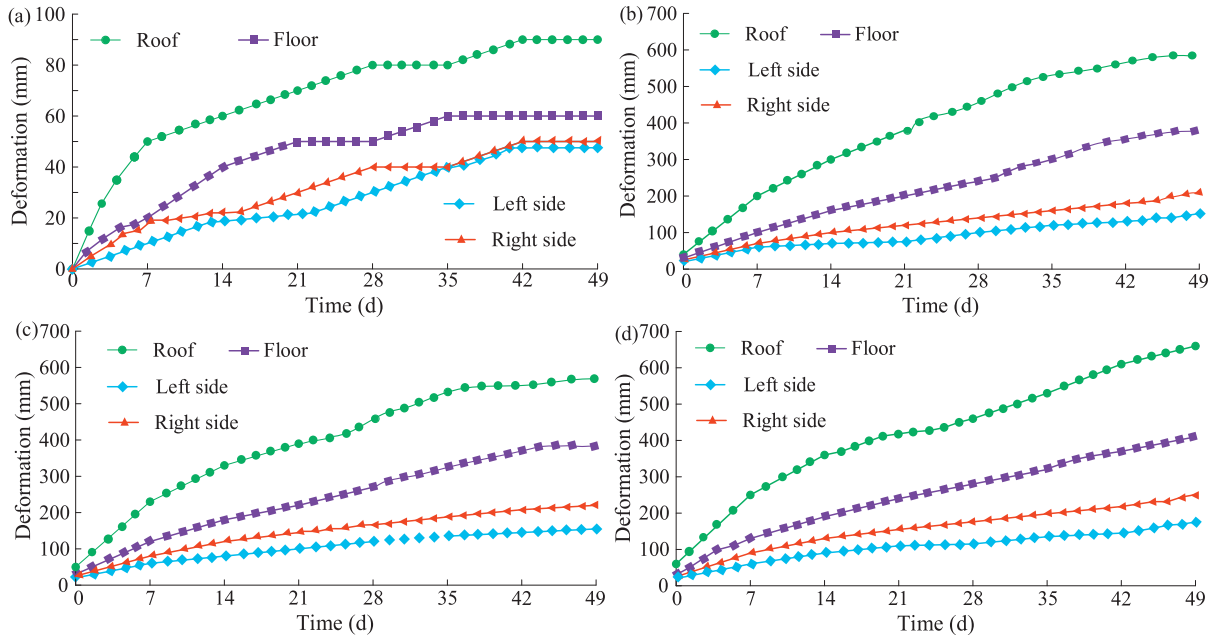

Fig. 9. Deformation characteristics of the surrounding rock in weakly cemented tunnels. (a) Deformation of measurement *A*, (b) deformation of measurement *B*, (c) deformation of measurement *C*, and (d) deformation of measurement *D*.

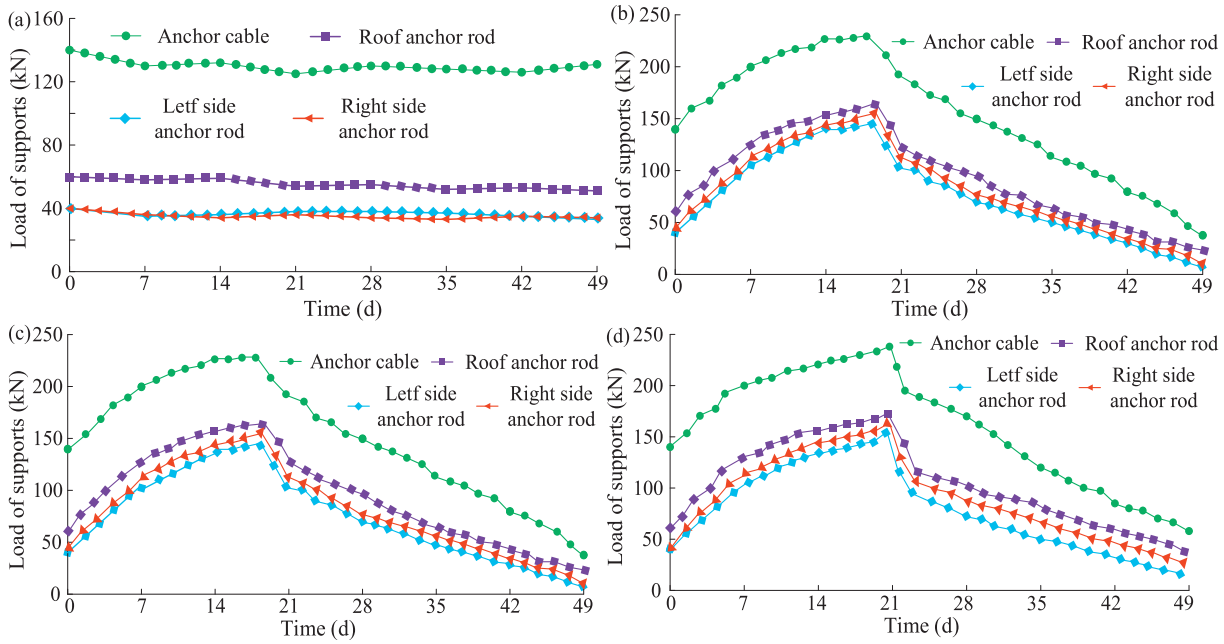

Fig. 10. Load characteristics of surrounding rock in weakly cemented tunnels. (a) Support loads in measurement *A*, (b) support loads in measurement *B*, (c) support loads in measurement *C*, and (d) support loads in measurement *D*.

and cables progressively diminishes over the period from 28 to 49 days, with the rate of reduction remaining relatively consistent throughout. Specifically, the anchor load decreases from 140 kN to 62 kN; the roof anchor rod load declines from 60 kN to 20 kN; and the side anchor rod load reduces from 40 kN to 15 kN. Initial analysis indicates that rock deformation accelerated significantly following the excavation of the rear tunnel, accompanied by a progressive increase in the load borne by anchor rods and cables. Once the deformation surpassed the capacity of the support system, the effectiveness of the anchor rods and cables in providing structural support diminished. Furthermore, owing to the asymmetric deformation of the tunnel, the reduction in load experienced by the anchor rods on the right side is greater than that observed on the left side.

Figure 11 illustrates the fracture characteristics of the roof. The failure of the roof can be categorized into four distinct regions: cracks, ruptures, relatively intact regions,

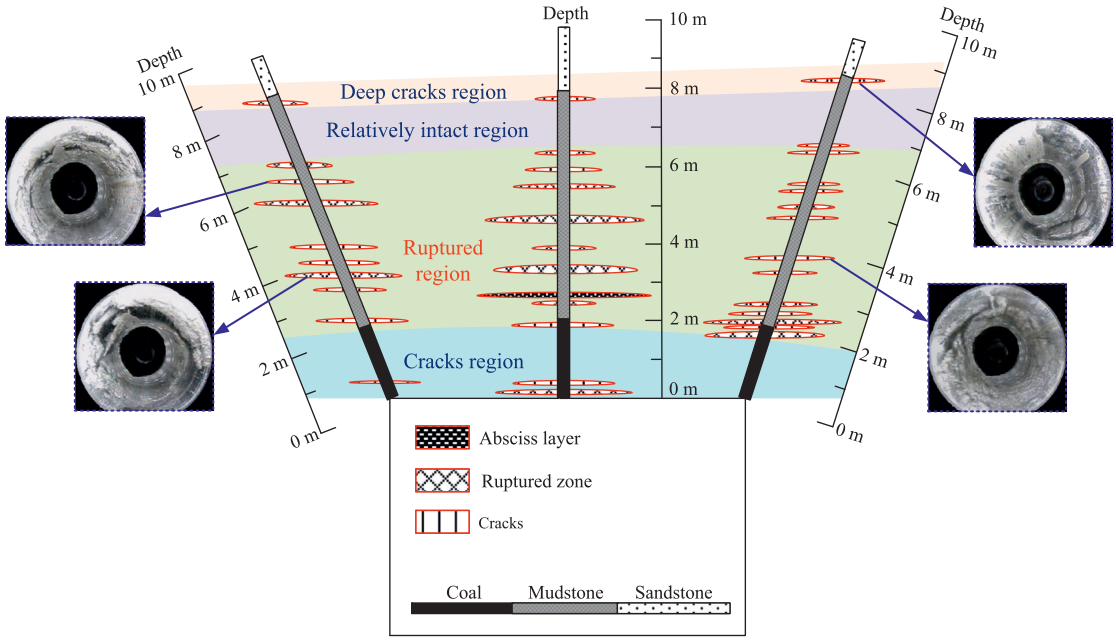

Fig. 11. Schematic of roof fracture characteristics.

and deep-crack regions. The crack region is located within the coal seam above the roof and exhibits a thickness of less than 2 m. The fractured zone is situated within the mudstone layer, exhibiting a thickness varying between 2 and 7 m. Above this, the relatively unaltered zone is found in the upper mudstone stratum, with an approximate thickness of 2 m. The region characterized by deep fissures is positioned at the interface between the mudstone and sandstone layers. Notably, the lower boundary of the fractured zone lies 1–1.5 m above the roof, a location susceptible to breaching through all mudstone strata and the coal seam, thereby potentially triggering roof collapse.

4 Combined layered control method of active and passive support

4.1 Stress distribution causing deformation of surrounding rock

To facilitate the calculation of stress distribution in Eq. (1) (Feng et al., 2022) during excavation, the polar coordinates for elastic mechanics are transformed into Cartesian coordinates, as expressed in Eq. (2) (Feng et al., 2022). In Eqs. (1) and (2), σ_x and σ_y represent horizontal stress and vertical stress, respectively. σ_r and σ_θ represent tangential stress and radial stress, respectively. r and θ represent radial coordinates and polar angles, respectively. $\tau_{r\theta}$ represents shear stress. a and q represent the tunnel radius and ground stress, respectively.

$$\begin{cases} \sigma_x = \frac{\sigma_r+\sigma_\theta}{2} + \frac{\sigma_r-\sigma_\theta}{2}\cos 2\theta - \tau_{r\theta}\sin 2\theta \\ \sigma_y = \frac{\sigma_r+\sigma_\theta}{2} - \frac{\sigma_r-\sigma_\theta}{2}\cos 2\theta + \tau_{r\theta}\sin 2\theta \end{cases}, \tag{1}$$

$$\begin{cases} \sigma_x = q - \frac{3qa^2}{2r^2}\cos 2\theta - q\cos 4\theta\left[\frac{a^2}{r^2} - \frac{3a^4}{2r^4}\right] \\ \sigma_y = -\frac{1}{2}\times\frac{qa^2}{r^2}\cos 2\theta + \frac{1}{2}q\cos 4\theta\left[\frac{2a^2}{r^2} - \frac{3a^4}{r^4}\right] \end{cases}. \tag{2}$$

As illustrated in Fig. 12, the impact of the excavation and support of the 2-1 tunnel within the #3 coal seam on the vertical stress distribution in the surrounding rock was examined. The incremental stress in the surrounding rock of the 2-1 tunnel was determined by calculating the difference between the superimposed and initial stresses through Eqs. (1)–(3). According to Fig. 12, the initial vertical ground stress measured 11.4 MPa when the roadways within the #2 and #3 coal seams were unexcavated. Upon excavation of the tunnel in the #3 coal seam without any support, the surrounding rock stress in the vicinity of tunnel 2-1 was 13.9 MPa, representing an increase of 21.9%. Following both excavation and subsequent support installation of the tunnel in the #3 coal seam, the surrounding rock stress near the 2-1 tunnel further increased by 0.9 MPa, reaching a total of 14.8 MPa.

Influenced by the stress disturbance caused by the previously excavated tunnel within the #3 coal seam, the vertical stress increment in the surrounding rock of the 2-1 tunnel—situated at a vertical distance of 27 to 45 m above—ranged from 2.1 to 4.0 MPa. This represents an increase of 20% to 45% relative to the initial geostress. Notably, when the 2-1 tunnel is positioned directly above the tunnel in the #3 coal seam, the vertical stress in the surrounding rock attains its maximum value. In summary, following the excavation of the tunnel in the #3 coal seam, the adjusted stress in the surrounding rock can be transmitted over a distance equivalent to 6 to 12 times the height of the roadway (Fig. 13).

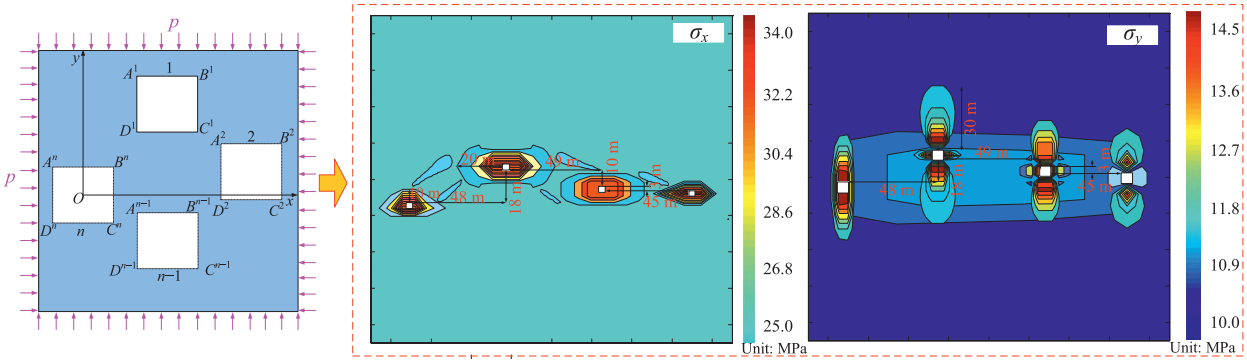

Fig. 12. Stress distribution model of the surrounding rock in adjacent caverns.

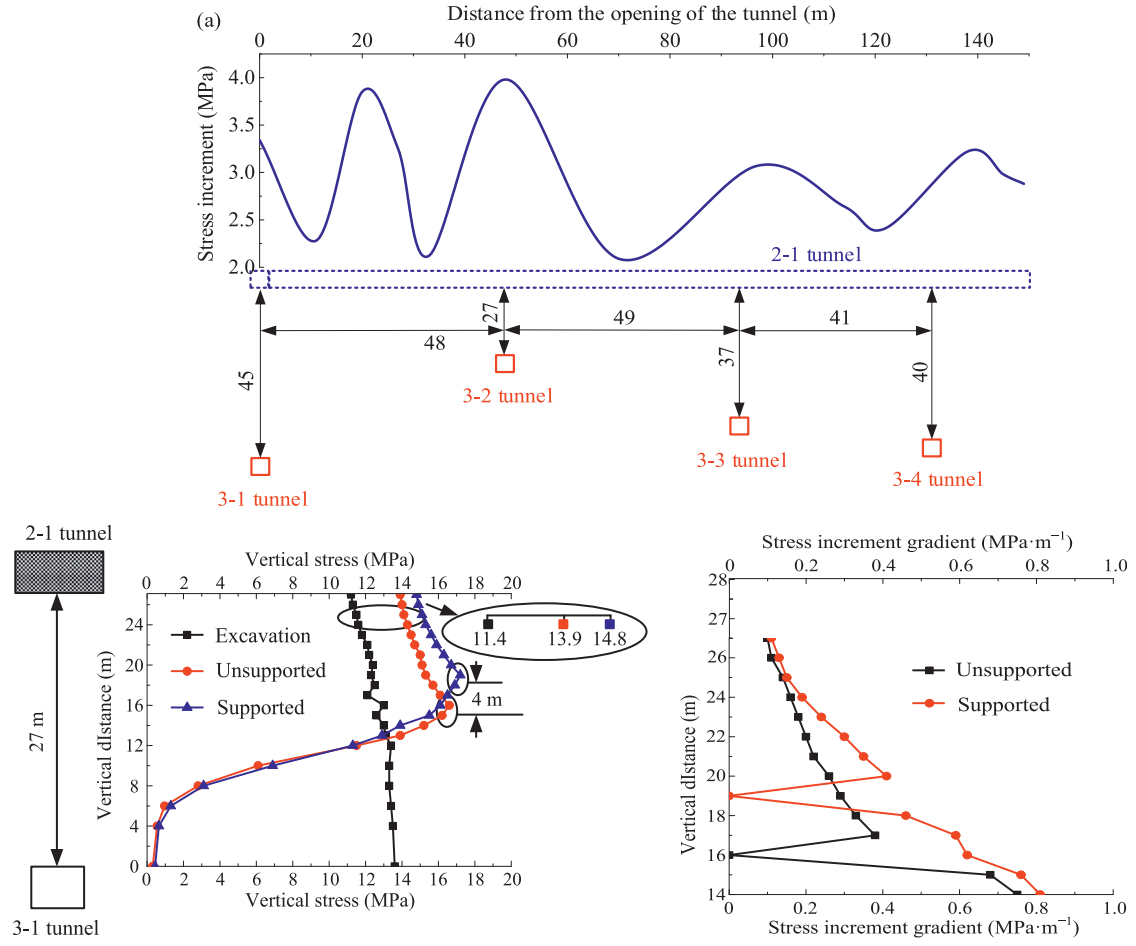

Fig. 13. Stress distribution of weakly cemented tunnels in adjacent caverns. (a) Characteristics of stress increment distribution, (b) vertical stress distribution, and (c) stress increment gradient distribution.

During the excavation of the 2-1 tunnel, the redistribution of stress induced the development of plastic zones within the surrounding rock mass. Letting the vertical stress at the location of the 2-1 tunnel be denoted as P_0, the surrounding rock is characterized by a cohesion c of 3.41 MPa and an internal friction angle φ of 30°. The tunnel excavation can be approximated by an equivalent radius r of 2 m. Under these conditions, the theoretical stress at the boundary of the tunnel cross-section is represented by P.

The equilibrium differential equation, excluding the effects of physical strength, is given by:

$$\frac{d\sigma_r}{dr} + \frac{\sigma_r - \sigma_\theta}{r} = 0. \tag{3}$$

The yield condition in the plastic zone of the 2-1 tunnel is determined by the Mohr–Coulomb (M–C) criterion:

$$\tau = c - \sigma_n \tan\varphi, \tag{4}$$

where τ is the shear stress, and σ_n is the normal force.

Expressing Eq. (4) in terms of principal stress ($\sigma_1 \geq \sigma_2 \geq \sigma_3$):

$$(1+\sin\varphi)\sigma_1 - (1-\sin\varphi)\sigma_3 = 2c\cos\varphi, \tag{5}$$

where σ_1 is the first principal stress, σ_2 is the second principal stress, and σ_3 is the third principal stress.

Then substituting $\sigma_1 = \sigma_r$ and $\sigma_3 = \sigma_\theta$ into Eq. (5) yields

$$(1+\sin\varphi)\sigma_r - (1-\sin\varphi)\sigma_\theta = 2c\cos\varphi. \tag{6}$$

Substituting Eq. (6) into Eq. (4)

$$\frac{\mathrm{d}\sigma_r}{\mathrm{d}r} - \frac{2\sigma_r\sin\varphi}{r(1-\sin\varphi)} = -\frac{2c\cos\varphi}{r(1-\sin\varphi)}, \tag{7}$$

and solving Eq. (7) for σ_r

$$\sigma_r = c\cot\varphi + cr^{\frac{2\sin\varphi}{1-\sin\varphi}}. \tag{8}$$

Substituting $(\sigma_r)_{r=r1} = -p$ (surrounding rock stress) into Eq. (8) yields

$$\begin{cases} \sigma_r = c\cot\varphi - (P + c\cot\varphi)\left(\frac{R}{r}\right)^{\frac{2\sin\varphi}{1-\sin\varphi}} \\ \sigma_\theta = c\cot\varphi - \frac{1+\sin\varphi}{1-\sin\varphi}(P + c\cot\varphi)\left(\frac{R}{r}\right)^{\frac{2\sin\varphi}{1-\sin\varphi}} \end{cases}. \tag{9}$$

Simplifying Eq. (9),

$$P = P_0(1-\sin\varphi) - c\tan\varphi. \tag{10}$$

In Eq. (10), P_0 represents the vertical stress at the tunnel location, whereas P denotes the stress at the boundary of the tunnel cross-section. The parameter φ corresponds to the internal friction angle of the surrounding rock, and c signifies the cohesion of the surrounding rock.

When a fracture zone occurs in the surrounding rock of the 2-1 tunnel, the critical value P_0 of the corresponding surrounding rock stress satisfies Eq. (11).

$$C_0\left(P_0 + \frac{\sigma_c}{K_1} + \frac{kK_2p}{k_p^2-1}\right) - \frac{2kp + 2\left(\sigma_c - \sigma_c^*\right)}{k_p^2-1} - \frac{\sigma_c^*}{K_1} = 0, \tag{11}$$

where σ_c represents the uniaxial compressive strength and σ_c^* represents the post peak strength of rock.

In Eq. (11), k_p is the triaxial stress coefficient; $k_p = (1+\sin\varphi) / (1-\sin\varphi)$; $K_1 = k_p - 1$, $K_2 = k_p + 1$.

$$C_0 = \frac{2}{K_2}\left(\frac{kp'}{kp' - \sigma_c - \sigma_c^*}\right)^{K_1/2}. \tag{12}$$

By substituting the relevant parameters into Eq. (12), the critical value of P_0 was determined to be 14.2 MPa. In the presence of a fractured zone within the surrounding rock of the 2-1 tunnel, the corresponding vertical stress was 14.2 MPa. Following excavation and the support operations in the #3 coal seam, the vertical stress in the surrounding rock of the 2-1 tunnel increased to 14.8 MPa, exceeding the critical vertical stress associated with the fractured zone, thereby inducing failure in the surrounding rock.

4.2 Determination of key support areas

As illustrated in Fig. 14, the active and passive layered support techniques for weakly cemented tunnels are categorized into two primary components: the external support system, which comprises high-prestressed anchor cables combined with grouting to seal the deep surrounding rock, and the internal support system, consisting of a U-shaped steel frame supplemented by flexible material filling and subsequent grouting to seal the shallow surrounding rock. The external bearing structure, established through the integration of high-prestressed anchor cables and grouting, fills the pores and fractures within the surrounding rock. This process results in the formation of a shell-like structure within the fractured soft rock. In conjunction with the tensioning effect imparted by high-prestressed anchor cables, the multi-layered shells are interconnected in series to form an integrated system that collaboratively bears loads and extends the support coverage. The internal bearing structure, composed of a U-shaped steel frame, is combined with grouting to seal the shallow surrounding rock, functioning as a rigid framework. Introducing flexible materials between the U-shaped steel frame and the rock enables the structure to withstand impact loads, thereby facilitating coupled coordination between the stress and deformation responses of the internal bearing system. The flexible material filling layer contributes a degree of uniform compressive stress across the entire tunnel cross-section, which mitigates localized stress concentrations and promotes a more evenly distributed load-bearing capacity throughout the section. Through the abovementioned active and passive layered support mechanisms, effective radial confinement is provided for weakly cemented rock masses, allowing the outer and inner support structures to work synergistically to accommodate some rock deformation by restricting it to within manageable limits.

Assuming that the internal load-bearing structure is subjected to a uniformly distributed circumferential pressure q, with radius r and thickness h, this study focuses on a weakly cemented tunnel section. Let M and N denote the bending moment and circumferential pressure at points A and B, respectively, while w_0 represents the radial displacement at these points. Considering that the segment ABD is in equilibrium under the critical load condition, the governing differential equation for bending is given by

$$\frac{\mathrm{d}^2w}{\mathrm{d}\theta^2} + w = -\frac{Mr^2}{\mathrm{EI}}. \tag{13}$$

Because $N = q \cdot \overline{AO}$, the torque at C is

$$M = M_0 + q\overline{AO} \times \overline{AF} - \frac{q}{2}\overline{AC}^2, \tag{14}$$

where M_0 is the initial value of M.

According to the graphic relationship of ACO,

$$\overline{OC}^2 = \left(\overline{AO} - \overline{AF}\right)^2 + \overline{AC}^2 - \overline{AF}^2. \tag{15}$$

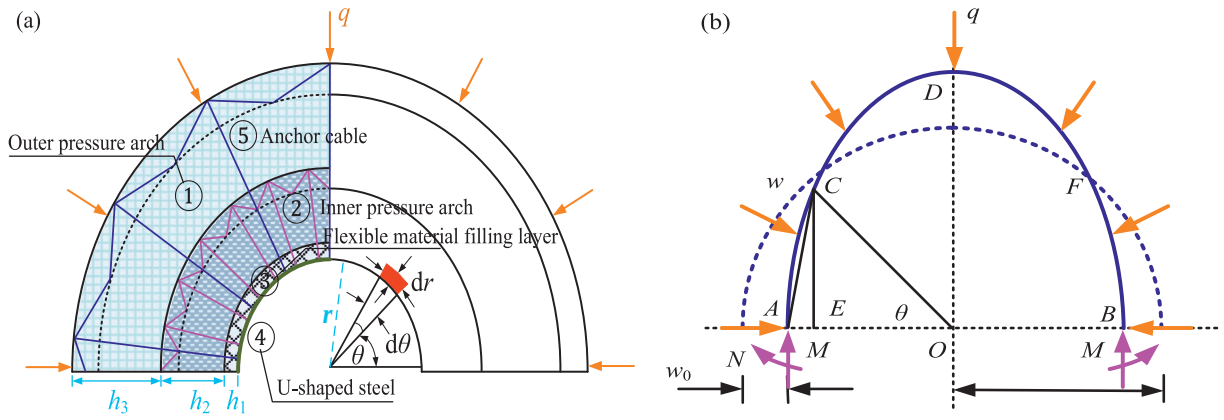

Fig. 14. Schematic of layered support for weakly cemented tunnel. (a) Structure model of layered support, and (b) theory model of layered support.

Substituting Eq. (15) into Eq. (14), based on $\overline{AO} = r - w_0$ and $\overline{OC} = r - w$,

$$M = M_0 - qr(w_0 - w). \tag{16}$$

Further substituting Eq. (16) into Eq. (14) and changing the flexural stiffness EI to G,

$$\frac{d^2w}{d\theta^2} + \left(1 + \frac{qr^3}{G}\right)w = -\frac{M_0 r^2 + qr^3 w_0}{G}. \tag{17}$$

According to

$$n^2 = 1 + \frac{qr^3}{G}, \tag{18}$$

$$w = A\sin n\theta + B\cos n\theta + \frac{-M_0 r^2 + qr^3 w_0}{G + qr^3}. \tag{19}$$

The boundary conditions at points A and D are:

$$\left(\frac{dw}{d\theta} + w\right)_{\theta=0} = 0, \tag{20}$$

$$\left(\frac{dw}{d\theta} + w\right)_{\theta=\frac{\pi}{2}} = 0. \tag{21}$$

Minimum critical failure load at $n = 2$, and

$$q_{max} = \frac{G}{r^3}(n^2 - 1) = \frac{Eh^3(n^2 - 1)}{12r^3(1 - \mu^2)}, \tag{22}$$

$$q_{max} = \frac{Eh^3}{4r^3(1 - \mu^2)}, \tag{23}$$

where n is the calculation constant, and μ is Poisson's ratio.

When the weakly cemented tunnel deforms, the U-shaped steel provides support force P_0 to the rock due to the contact between the inner bearing structure and the surrounding rock. When the failure stress P_k of the rock is lower than the minimum bearing capacity q_{max} of the inner bearing structure and the support reaction force P_0 of the U-shaped steel, the weakly bonded roadway is in a stable state.

During deformation of a weakly cemented tunnel, the U-shaped steel exerts a support force P_0 on the surrounding rock through contact between the inner bearing structure and the rock mass. Stability of the weakly bonded roadway is maintained when the failure stress P_k of the rock is less than the lesser of the maximum bearing capacity q_{max} of the inner bearing structure and support reaction force P_0 provided by the U-shaped steel.

$$P_k < q_{max} + P_0. \tag{24}$$

4.3 Quantitative determination of support parameters

To investigate the compressive behavior of the buffer layer, a numerical simulation was performed focusing on the deformation of weakly cemented tunnels. A finite difference numerical model was developed, as illustrated in Fig. 15. Given that the primary role of the buffer layer is to mitigate stress concentration within the U-shaped steel frame, the buffer layer thicknesses were specified as 0.1 and 0.3 m.

The numerical model size is 50 m (height) × 50 m (width) × 30 m (thickness). The surrounding rock grid within the blue solid line range in Fig. 15 is dense, and suitable grids are selected for the rock masses. The constitutive behavior of the numerical model is represented by the M–C model, whereas the joint constitutive behavior is characterized using the Coulomb slip model implemented as a surface contact. Utilizing the derived rock physical and mechanical parameters alongside the geostress test data, the boundary conditions are defined as follows: the top boundary is subjected to a uniformly distributed stress of 10 MPa; both lateral boundaries are assigned a uniformly distributed stress of 5 MPa; a uniformly distributed stress of 15 MPa is imposed on the front and rear boundaries; and the bottom boundary is constrained as a fixed boundary. The calculation results are shown in Figs. 16 and 17.

The findings indicate that the buffer layer undergoes substantial compressive deformation. Specifically, the maximum compressive strain observed in the right shoulder and side wall approaches 90%, whereas the left side wall of the buffer layer experiences a compressive strain of up to 70%. The maximum convergence of the U-shaped steel frames remains below 0.05 mm, suggesting that the buffer

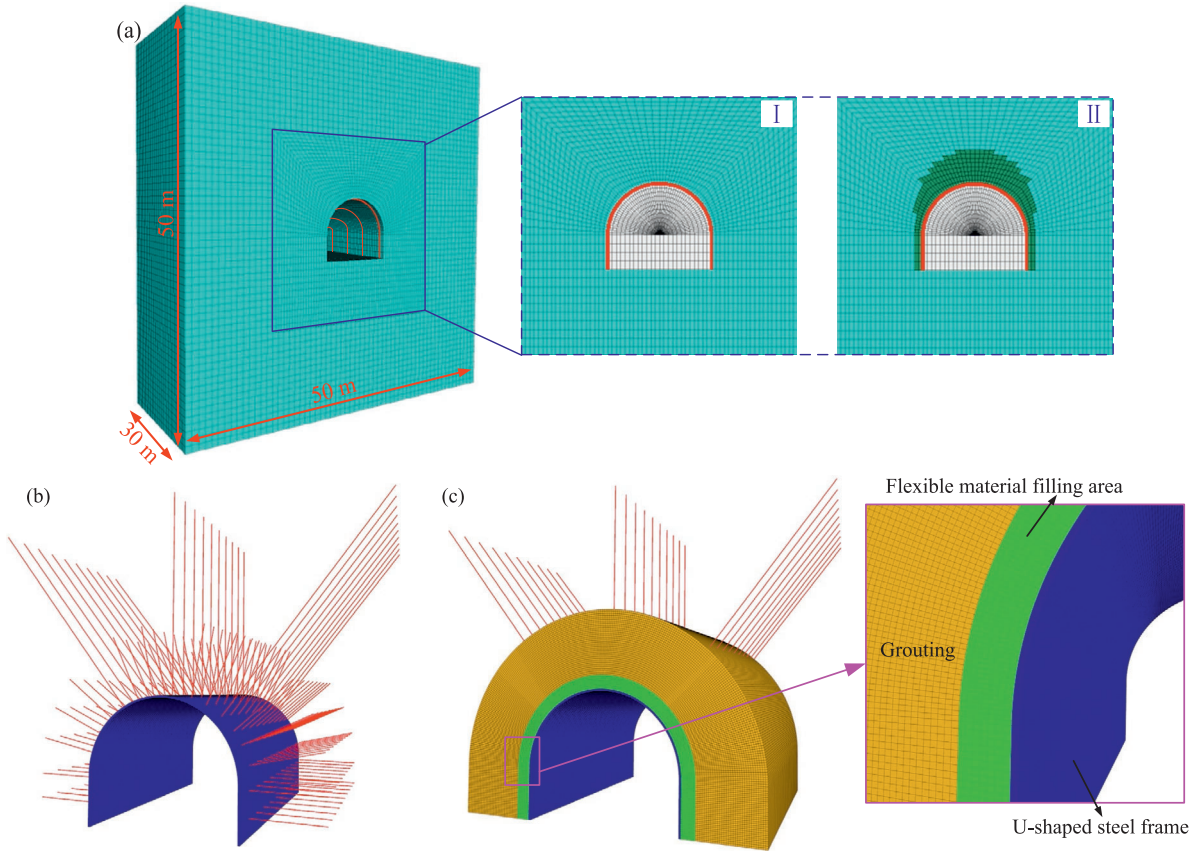

Fig. 15. Numerical model of secondary support. (a) U-shaped steel frame + flexible material filling, (b) anchor rod + anchor cable, and (c) grouting reinforcement.

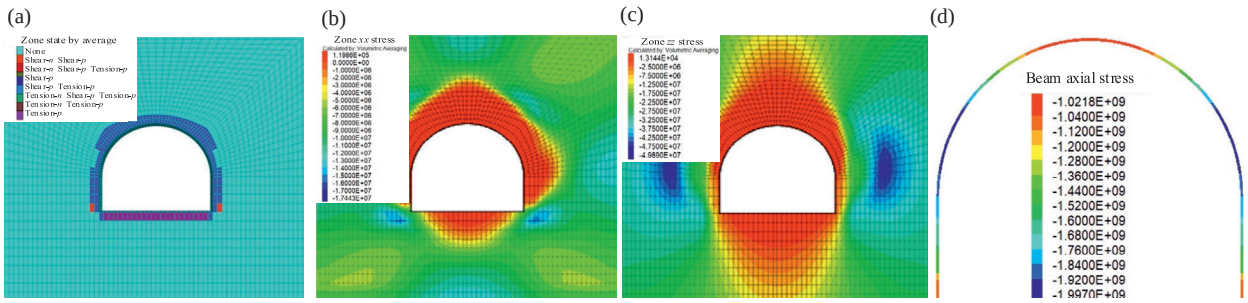

Fig. 16. Filling thickness between the U-shaped steel frame and surrounding rock of 0.1 m. (a) Plastic zone, (b) horizontal stress, (c) vertical stress, and (d) axial force.

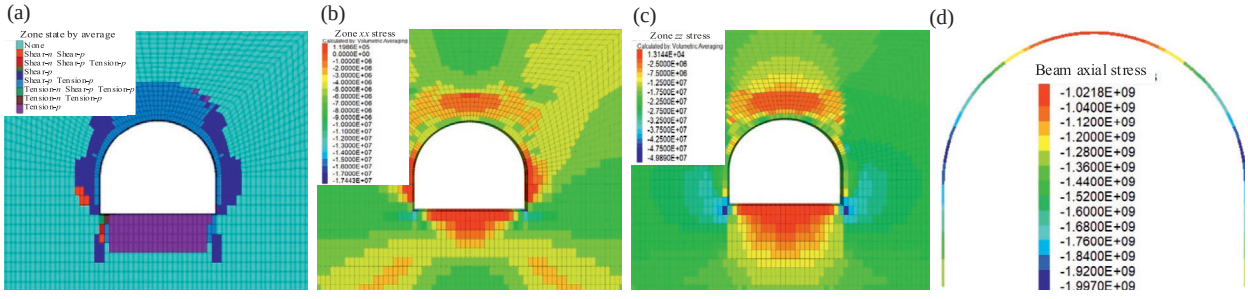

Fig. 17. Filling thickness between the U-shaped steel frame and surrounding rock of 0.3 m. (a) Plastic zone, (b) horizontal stress, (c) vertical stress, and (d) axial force.

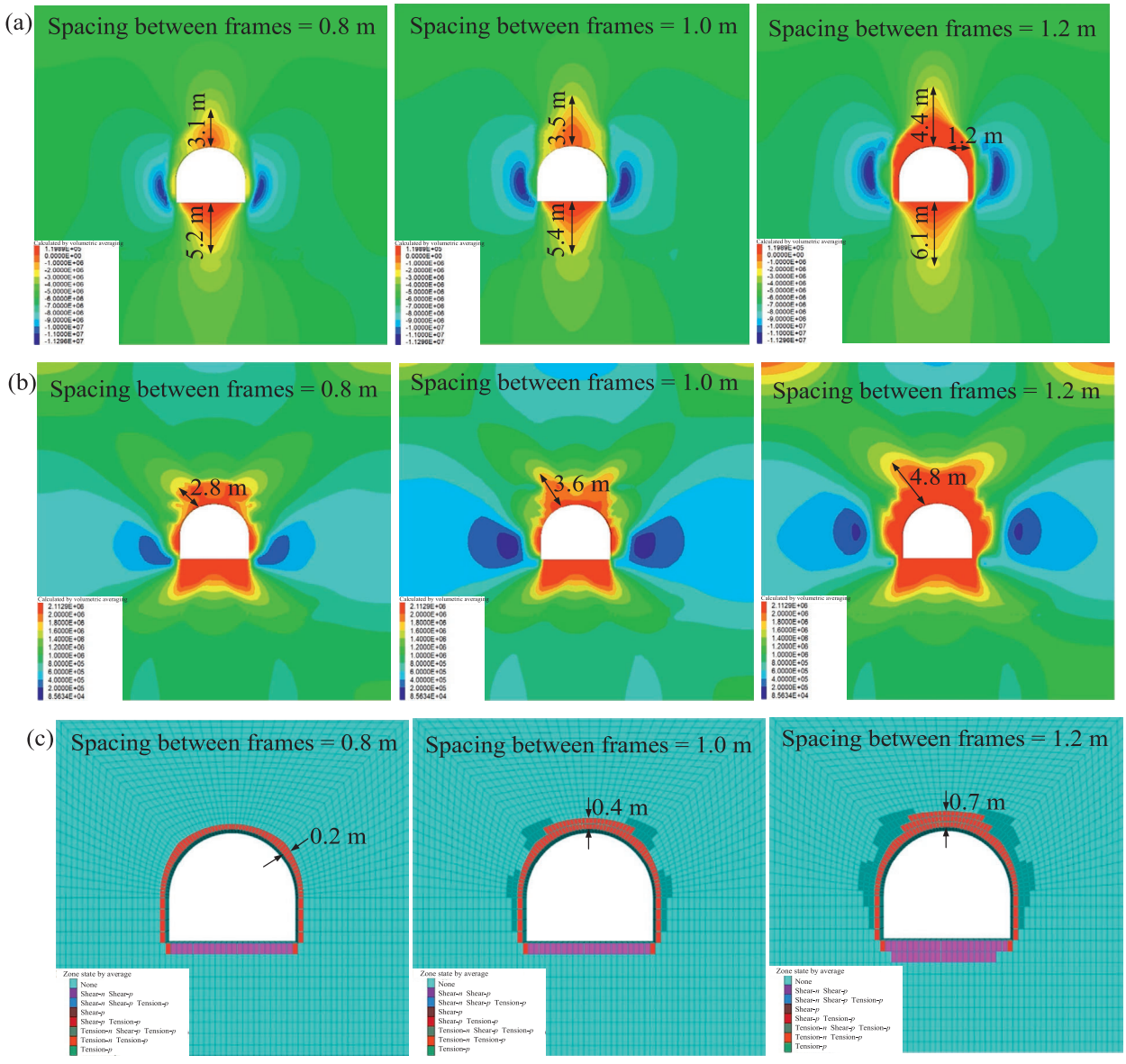

Fig. 18. Different spacings between U-shaped steel frames. (a) Vertical stress, (b) horizontal stress, and (c) plastic zone.

layer predominantly accommodates the time-dependent deformation of the surrounding rock. Furthermore, the incorporation of buffer layers results in a reduction of the peak stress directly exerted on the U-shaped steel frames from 3.45 MPa to 1.75 MPa. Additionally, the axial force distribution length exceeding 200 kN decreases from 5.35 m to 3.15 m.

As illustrated in Fig. 18, the vertical stress, horizontal stress, and plastic zone distribution patterns of U-shaped steel frames with spacings of 1.0, 1.5, and 2.0 m exhibit similar characteristics, all demonstrating extensive concentration. Compared with frame spacings of 1.5 and 2.0 m, reducing the spacing to 1.0 m results in a decrease in the vertical stress distribution range by 15% and 60%, respectively, and a reduction in the horizontal stress distribution range by 20% and 90%, respectively. These findings suggest that decreasing the spacing between U-shaped steel frames enhances their load-bearing efficiency. The differences in stress for range reduction and plastic zone control for spacings of 1.5 and 2.0 m are less pronounced, ranging from 20% to 45%. To ensure tunnel safety while minimizing construction costs, a support scheme employing a U-shaped steel frame spacing of 1.5 m was selected.

Figure 19 illustrates the plastic zone of the surrounding rock under varying grouting range conditions. With the expansion of the grouting range, the height of the plastic zone within the roof rock is markedly reduced, whereas the failure depth on both sides maintains a consistent width of 2 m. When the grouting range of the roof rock is 3 m, the difference in distribution height of the plastic zone between the rock layers within the grouting range and nearby area is significant, reaching more than 100%. When the grouting within the roof rock layer extends to 4 m, a marked reduction in the plastic zone above the roof is observed. Increasing

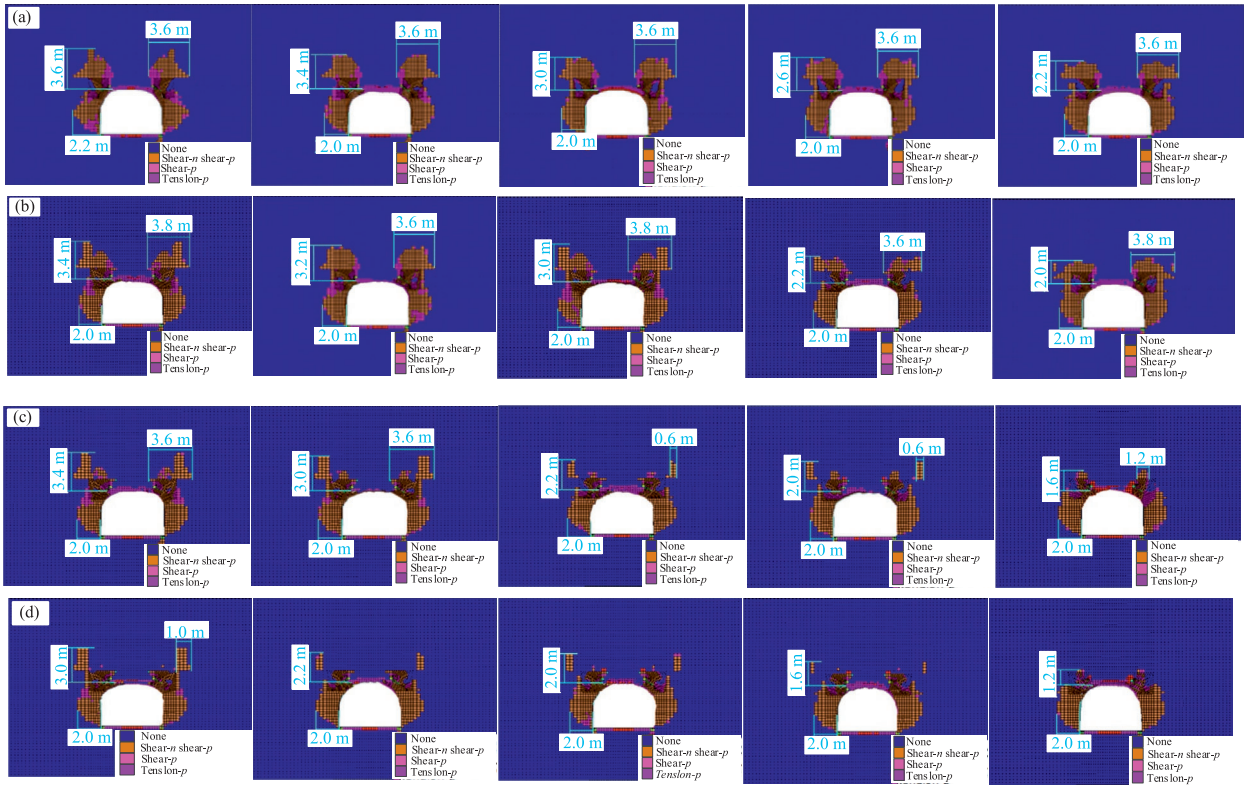

Fig. 19. Plastic zones with different grouting ranges for the roof. (a) Grouting range of 2 m, (b) grouting range of 4 m, (c) grouting range of 6 m, and (d) grouting range of 8 m.

the grouting range to 6 m results in the plastic zone being segmented into two discontinuous regions. In this scenario, the height of the plastic zone beyond the grouted area exceeds 1.6 m, whereas its horizontal distribution width remains limited to 0.6 m. At an 8-m grouting range, the grouted area exceeds the width of the plastic zone in the surrounding rock, leaving only a minor plastic zone within the roof rock layer adjacent to the tunnel shoulder.

4.4 Design of rigid flexible coupling support scheme

This study proposes a support strategy comprising an initial immediate support phase followed by a secondary controlled support phase, to address the features of substantial deformation and critical timeliness, as illustrated in Fig. 20. Upon excavation of the 2-1 tunnel, prompt implementation of support measures was required, with

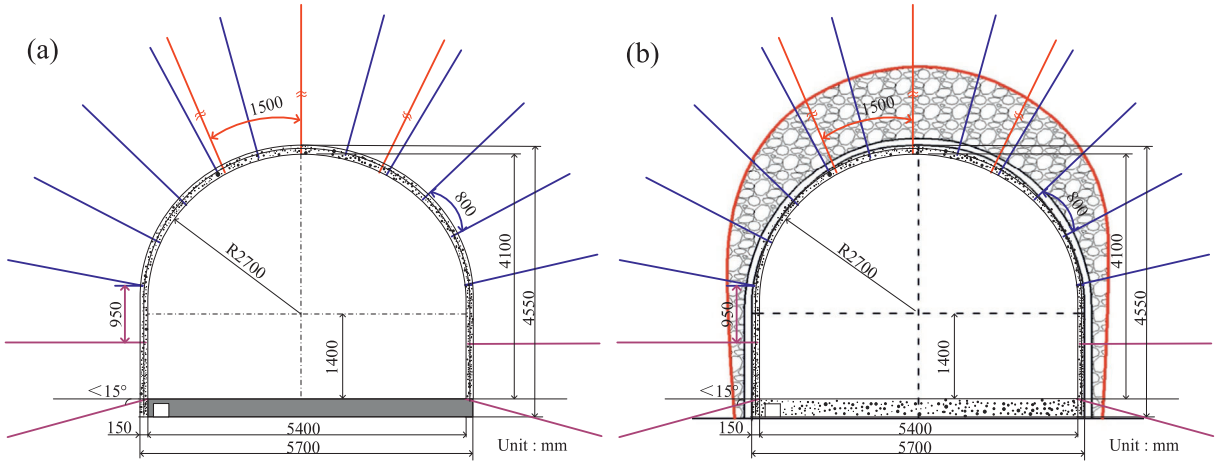

Fig. 20. Schematic of weakly cemented tunnel support. (a) Primary support, and (b) secondary support.

the primary support system consisting of anchor rods, anchor cables, anchor mesh, and shotcrete. When the tunnel deformation exceeded the control capacity of the primary support system, a secondary support, comprising U-shaped steel arches and a buffer layer, was implemented. The U-shaped steel arch utilizes retractable connection joints to enhance its deformation coordination capabilities, thereby ensuring a stable load-bearing capacity of the surrounding rock structure during joint deformation. The minimum design thickness of the buffer layer was greater than 0.5 m, primarily employing bagged pebbles to accommodate the time-dependent deformation of the sur.

The diameters of the pebbles utilized in the on-site buffer layer ranged from 0.09 to 0.12 m with densities between 2.45 and 3.15 g/cm^3. Each bag of pebbles weighed approximately 100 kg. The overall compression process can be categorized into distinct phases, namely yielding, elasticity, and compaction (Fig. 21). I represents the void compaction stage, II represents the crack compaction stage, and III represents the overall compaction stage. ε_c and ε_p represent the void compaction strain limit and crack compaction strain limit, respectively.

During the initial phase, the deformation of bagged pebbles primarily results from the compression of the voids between the pebbles. Consequently, the increase in stress throughout this stage is relatively modest, and the rate of stress escalation is lower compared to that observed in the elastic and densification phases. The stress experienced by bagged pebbles during the elastic phase exhibits a linear increase in response to compressive strain. Additionally, most of the volume reduction in bagged pebbles occurs predominantly within this elastic stage. When the compression of the interstitial spaces between the pebbles during the compaction phase is finalized, the strain observed in the bagged pebbles primarily results from the compression of the pebble matrix itself. Consequently, the stress exhibits a rapid increase corresponding to the strain rate. Notably, the bagged pebbles remain structurally intact after traversing the compaction zone, showing no evidence of fragmentation or damage.

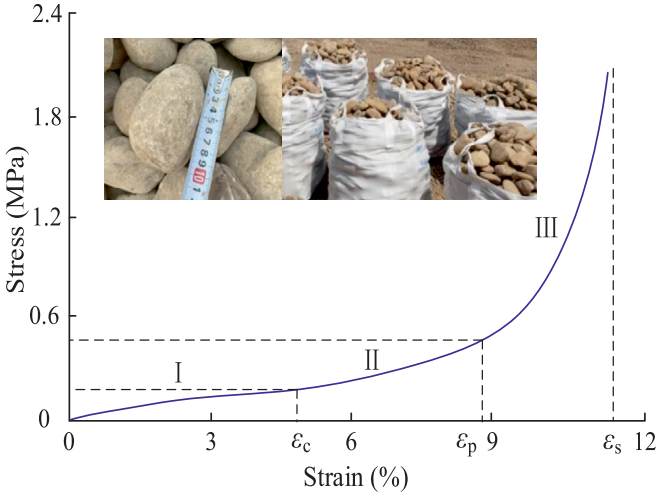

Fig. 21. Stress–strain curve of bagged pebbles.

The U-shaped steel arch employs a retractable connection technique. This method generates an initial normal force via bolt pre-tensioning, while the friction at the joint contributes to the support capacity of the arch (Fig. 22). Upon applying a compressive load to the U-shaped steel arch, the axial force progressively intensifies. Once the joint attains its maximum frictional resistance, shrinkage deformation is initiated. As a result of the contraction occurring between the U-shaped steel arches, the axial force experienced by the joint bolts progressively increases. Consequently, the contraction of the U-shaped steel arches does not result in a reduction of their load-bearing capacity. During the installation process, the U-shaped steel arch was fitted with two adjustable joints, each allowing a maximum contraction of 0.25 m. The initial pre-tightening torque applied to the bolts of the reducible joints was established as 100 N·m. The horizontal spacing between the U-shaped steel arches was maintained at 1 m. Following the implementation of primary support in the 2-1 tunnel, the construction of the U-shaped steel arch and buffer layer was initiated once the deformation exceeded the allowable deformation threshold of the U-shaped steel arch, as illustrated in Fig. 17.

The grouting support strategy employs an integrated approach combining both shallow and deep grouting techniques. The grouting mixture consisted of cement combined with water glass. The cement utilized in this study was of the P.C 32.5 grade. A water-to-cement ratio of 0.5∶1 was employed, with the addition of 6% admixture by weight. The water glass used had a modulus (M) ranging from 2.8 to 3.1, and its concentration varied between 38 and 400 Bé. The volumetric ratio of cement to water glass solution was maintained at 1∶1. The dispersion extent of the slurry in both shallow and deep regions measured 3 m. The objective of shallow grouting is to effectively seal delamination and fractures occurring within the superficial strata. The primary purpose of deep grouting is to enhance the stability of the surrounding rock mass. For shallow grouting, boreholes were configured in a "5-4-5" arrangement, with a spacing of 1.25 m × 1.25 m and a penetration depth of 3 m. In contrast, deep grouting boreholes follow a "3-2-3" pattern, with a spacing of 2.6 m × 2.6 m and a depth extending to 5.5 m.

Table 3 presents the parameters for the secondary support of the 2-1 tunnel. To improve the stability of the U-shaped steel arches along the tunnel axis, adjacent arches were interconnected using channel steel tie rods and reinforced with welded mesh composed of round steel bars measuring Φ6.5 mm × 100 mm × 100 mm. The base of the U-shaped steel arch was embedded within a 0.3-m-thick concrete slab. The reinforcement framework of the concrete floor consisted of a welded steel wire mesh composed of Φ6.5 mm steel bars and #12 I-beams. Following the installation of the buffer layer and the U-shaped steel

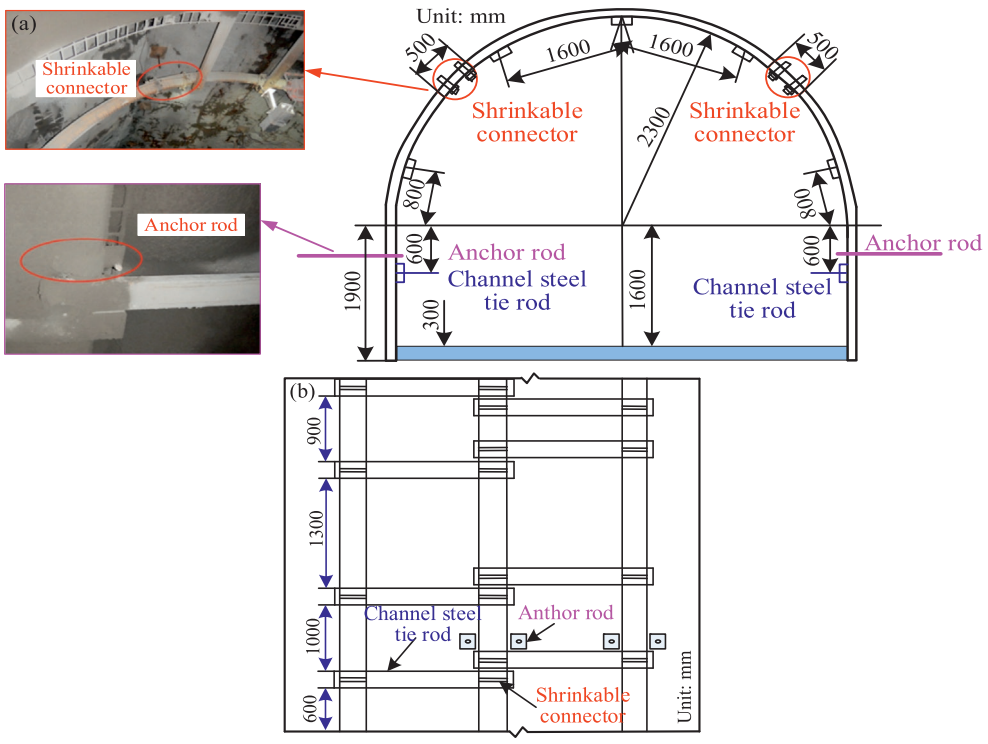

Fig. 22. Schematic of secondary support for weakly cemented tunnel. (a) Schematic of tunnel support cross-section, and (b) side view of tunnel support.

Table 3
Support mode of swelling soft rock.

Support position	Support form	Effect analysis
Roadway section	U-shaped steel shed	Load evenly and ensure the shape of the roadway section
Between the surrounding rock and U-shaped steel shed	Filling behind the U-shaped steel shed	Releasing pressure
Legs of U-shaped steel shed	Shed anchor	Restrain the deformation of U-shaped steel shed
Floor	Laying steel mesh + concrete floor	Restrain the deformation of U-shaped steel shed
Roadway surface	Shotcrete	Protect supporting structure
Surrounding rock	Sweep roof and floor + repair the anchor rod	Clean up broken rock and restrain the deformation of U-shaped steel shed

arch, a 1-m thick layer of concrete was sprayed onto the structure.

4.5 Analysis of application effectiveness

To investigate the influence of support, four monitoring zones were established within the 2-1 tunnel, designated as zones #1, #2, #3, and #4. Each adjacent monitoring zone was spaced 50 m apart. Within each zone, monitoring points were installed to measure surface displacement as well as anchor rod forces. Anchor rods located at or near the midpoint between the two sides of the tunnel should be selected as monitoring points within the designated monitoring section. The monitoring points on both sides of the tunnel were installed in rows corresponding to the anchor rods. The anchor rod located at the central or adjacent position of the tunnel roof was selected as the designated roof monitoring point, and the floor monitoring point was positioned directly beneath this roof monitoring location. The anchor rod force gauge was positioned at the center of the alley for measurement purposes, with the anchor rod force gauge utilized as the monitoring device. Furthermore, a borehole inspection imaging device was employed in proximity to the anchor rod location at the right shoulder corner of monitoring section #2 within the tunnel, achieving a borehole observation depth of 5 m. Figure 23 shows the displacement monitoring curves of the roof and floor, as well as the surrounding rocks on both sides. The displacement exhibits a gradual increase as the monitoring duration is extended. After more than 50 days of observation, the displacement appears to approach a stabilization phase. The cumulative deformation recorded for the two groups ranges from 29 to 37 mm, whereas the overall cumulative deformation spans from 34 to

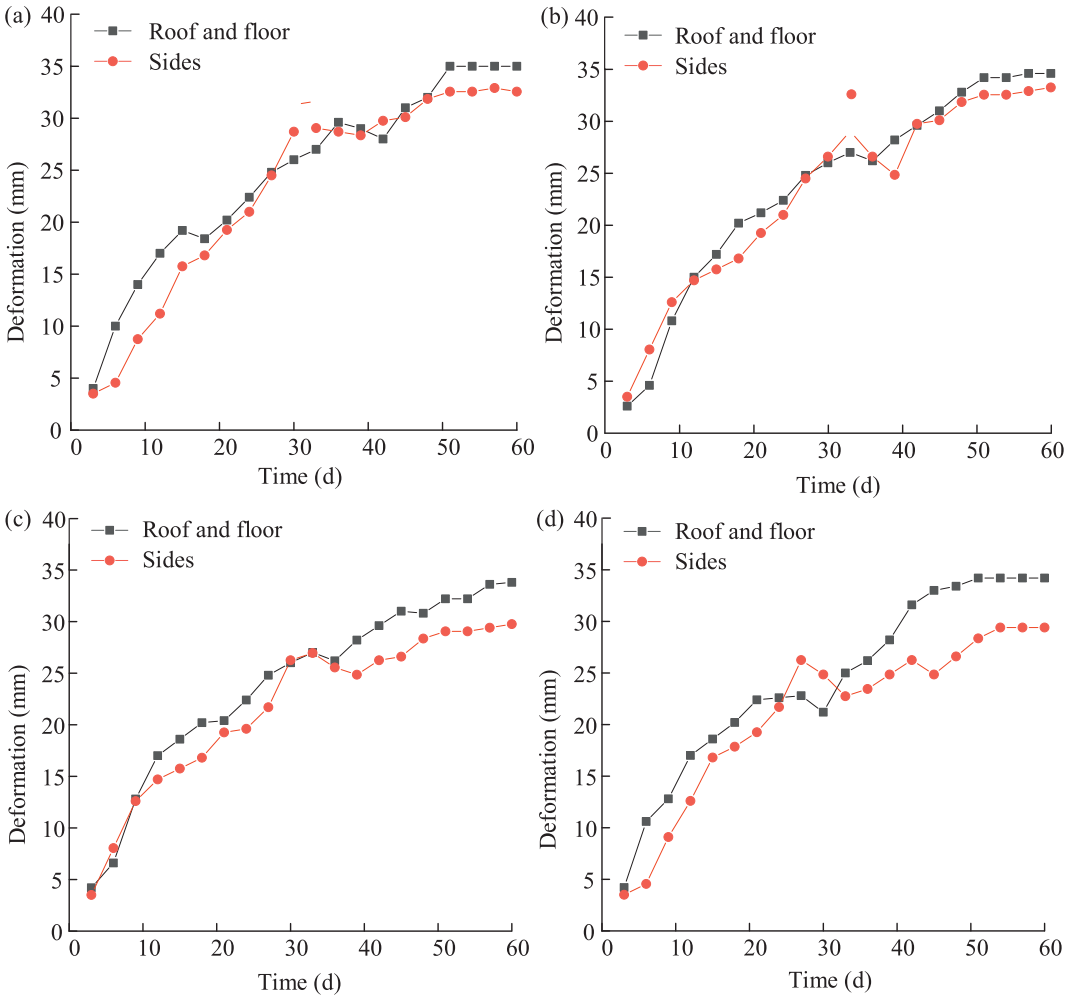

Fig. 23. Surface displacement monitoring curve of weakly cemented tunnel. (a) #1, (b) #2, (c) #3, and (d) #4.

39 mm. The displacement is significantly diminished in comparison to the period prior to the implementation of anchoring control support, and the deformation of the tunnel rock mass remains relatively minimal. This suggests that the secondary support system exerted an effective control influence.

Figure 24 illustrates the force monitoring curve of the anchor bolts located on the side of the 2-1 tunnel. The data indicate an initial rapid increase in force, followed by a stabilization phase as the monitoring duration progresses. The maximum tensile force observed in the anchor rods on the left side is 131.7 kN, whereas that on the right side reaches 146.5 kN. All monitored anchor rods attained or exceeded the designed anchoring capacity of 100 kN, demonstrating that the anchor rods are functioning within their intended support parameter range. Moreover, these results suggest that the implementation of the control support method in weakly cemented tunnels effectively enables the anchor rods to provide adequate support, thereby ensuring satisfactory support and control performance.

Figure 25 presents a comparative visual analysis of the surrounding rock adjacent to the anchor rod located at the right shoulder corner of the 2-1 tunnel, captured at the identical position prior to and following a 60-day observation period. The original rock fissures within the 0–6 m range were filled with grouting slurry, resulting in the surrounding rock being largely intact. An analysis of the displacement in the 2-1 tunnel, force variations in the two lateral anchor rods, and crack characteristics observed through drilling indicate that a U-shaped steel arch combined with a buffer layer for secondary support substantially reduces the deformation of the surrounding rock in the weakly cemented tunnel. Furthermore, this approach effectively controls deformation along the tunnel sides. The support performance of the tunnel is illustrated in Fig. 26.

5 Discussion

The effectiveness of the grout is a critical factor that influences the overall grouting outcome. The chosen slurry material was P.F 32.5 cement, prepared with water-to-cement ratios of 0.50, 0.75, 1.00, 1.25, and 1.50. Within the water-to-cement ratio range of 0.50 to 1.00, the viscos-

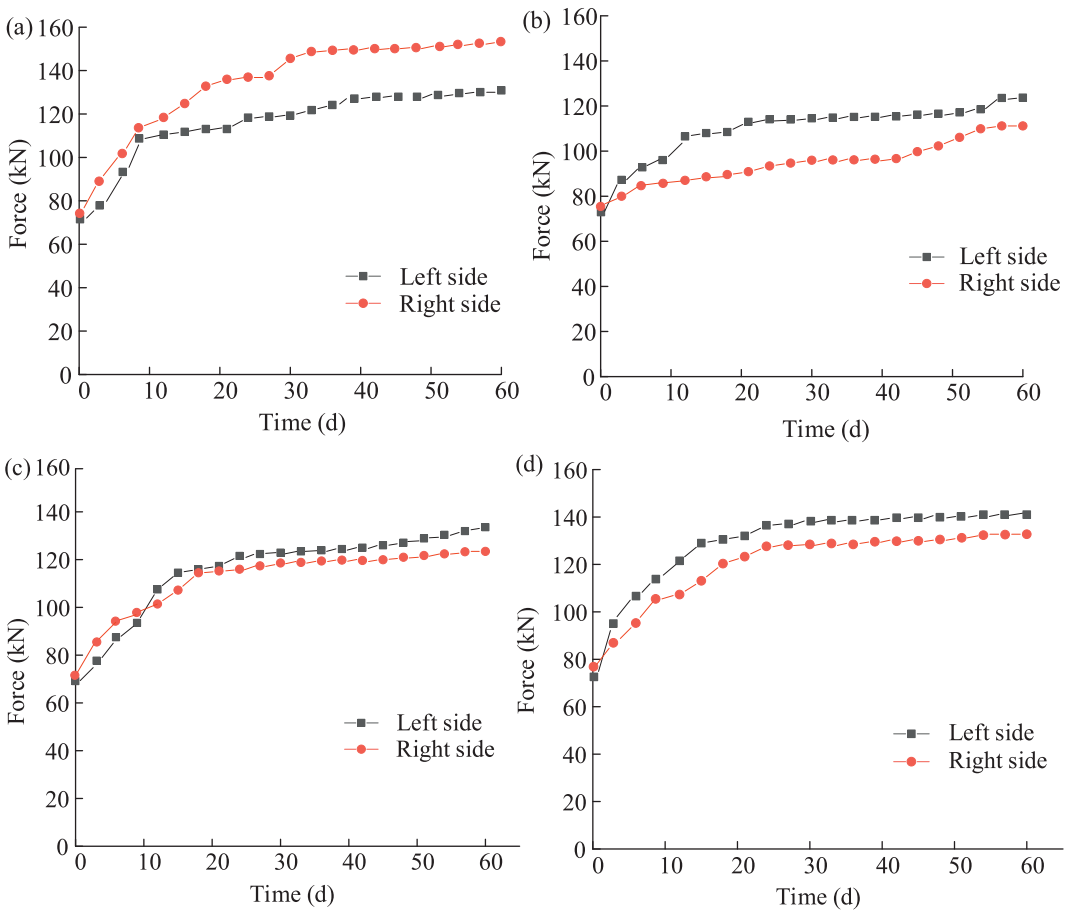

Fig. 24. Force monitoring of the bolt in the middle of the two sides of the newly excavated tunnel. (a) #1, (b) #2, (c) #3, and (d) #4.

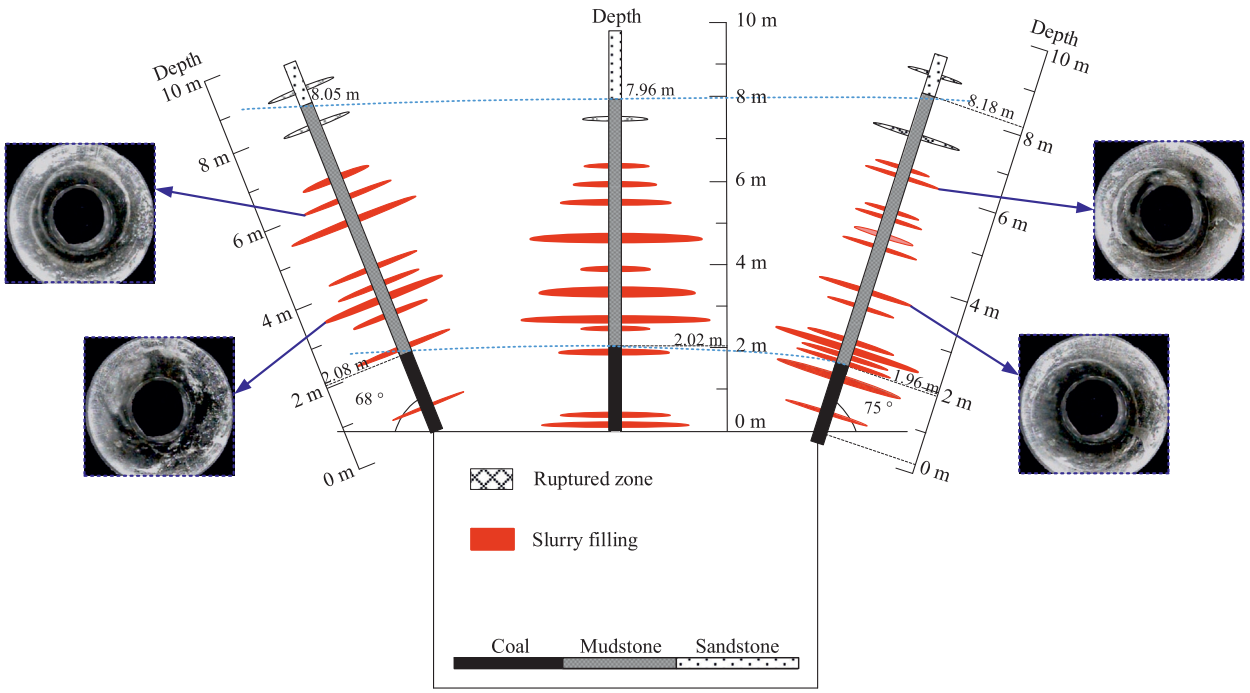

Fig. 25. Peek-ahead comparison map of internal drilling in weakly cemented surrounding rock.

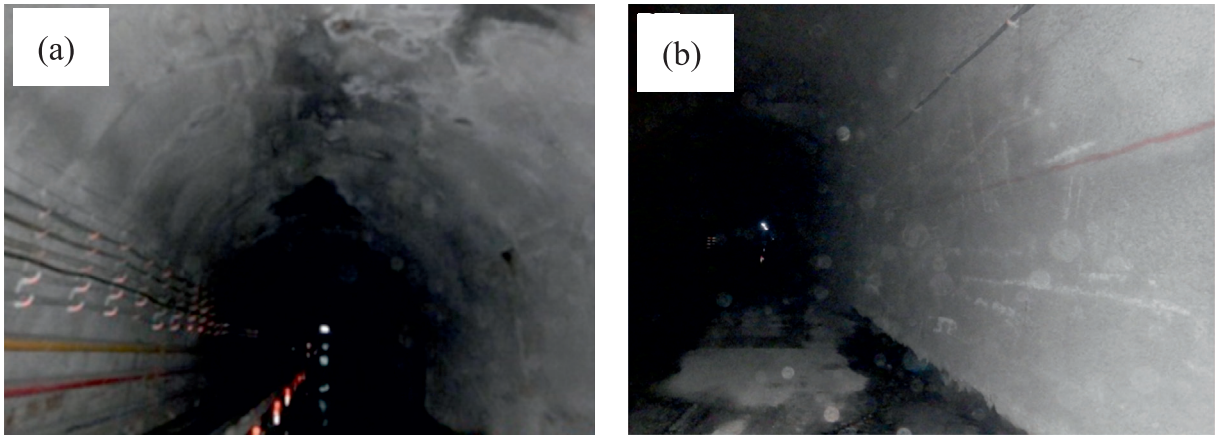

Fig. 26. Effect drawing of surrounding rock support of weakly cemented tunnel. (a) Overall support effect of the tunnel, and (b) effect of alley support.

Fig. 27. Failure test of grouting reinforcement rock.

ity of the slurry exhibited a rapid decline as water content increased. For ratios of 1.00 to 1.50, the reduction in slurry viscosity occurred at a diminished rate. Conversely, at ratios below 0.50, the slurry demonstrated higher viscosity, which impedes its diffusion. Additionally, the rate of water separation from the slurry was approximately linearly correlated with the water-to-cement ratio. For water-to-cement ratios below 0.50, the slurry exhibited poor fluidity. For ratios exceeding 1.25, the slurry's water separation rate exceeded 30%. Therefore, it is recommended that the water-to-cement ratio during grouting be maintained within the range of 0.50 to 1.25.

The uniaxial compressive strength of rock reinforced through grouting exhibits a decline as water-to-cement ratio increases. This reduction is primarily attributed to the elevated water content in the grout mixture, which leads to a decrease in the overall density of the rock. The yield point on the stress–strain curve for rocks with a high water-cement ratio is not particularly pronounced, and the reduction in stress following the peak is comparatively minimal. This observation suggests that the homogeneity of rocks reinforced through grouting is greater than that of natural, unreinforced rocks. The predominant modes of failure in grouted reinforced rocks are tensile or unidirectional inclined shear failure (Fig. 27).

At a ratio of 0.75 and a water glass to cement volume ratio of 0.2:1, the bonding rate was observed to be the slowest (Fig. 28). In contrast, the gelation rate reached its maximum when the volume ratio was 0.1:1. When the volume ratio exceeded 0.2:1, the gelation time of the slurry diminished with increasing volume ratio, with a progressively declining rate of deceleration. At low concentrations of water glass, the mixture tended to exhibit poor homogeneity, with elevated levels of water glass resulting in a pronounced dilution effect on the cement slurry. The reinforcement effect of grouting on rocks demonstrated a progressive pattern, initially intensifying and subsequently diminishing as the volume ratio of water glass cement increased. A low concentration of water glass corresponds to a reduced extent of the hydration reaction with cement, which leads to a decrease in the compressive strength of the rock. Conversely, as the water glass content increases, the degree of the hydration reaction is enhanced, resulting in a corresponding improvement in the rock's compressive strength. When the volume ratio of water glass to cement exceeds 0.2:1, the dilution effect on the composite slurry progressively intensifies as the water glass content increases, resulting in a reduction in the strength of the rock.

6 Conclusions

(1) The bagged pebbles employed in the buffer layer support exhibited excellent compressive properties, enabling them to effectively accommodate the time-dependent deformation of the surrounding rock mass

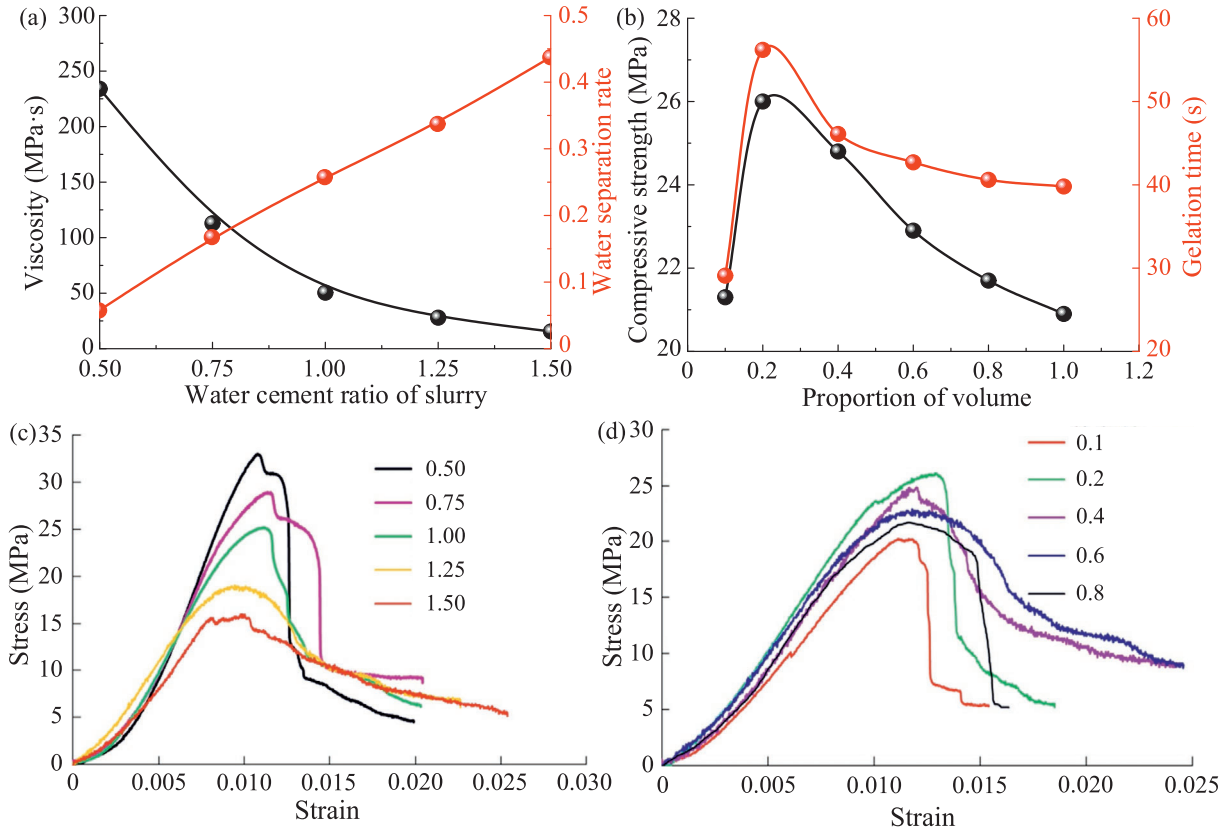

Fig. 28. Testing for grouting reinforcement of rocks with different ratios of water, cement, and volume. (a) Viscosity and water separation rate, (b) gelation time and compressive strength, (c) different water cement ratios, and (d) different volume ratios.

and consequently mitigate the deformation stress exerted on the U-shaped steel arch. When employing a buffer layer, the U-shaped steel arch experienced circumferential compression, characterized by an average compressive stress below 1.75 MPa. The highest compressive stress was observed at the right-side wall and shoulder region of the U-shaped steel arch.

(2) When pebbles were employed as backfill material, the axial force within the U-shaped steel arch exhibited a decreasing trend both upward and downward from the arch shoulder. The maximum axial force was observed at the arch shoulder, whereas the minimum occurred at the arch crown. Additionally, the axial force measured at the base corresponded to 64% of the axial force at the arch shoulder. The maximum bending moment in the U-shaped steel arch occurred at three-quarters of the height of the side wall.

(3) The mechanical strength of grouted rock progressively improved as the duration of the grouting process was extended. At a volume ratio of 0.2:1, the water glass cement slurry demonstrated the slowest rate of bonding; however, it achieved the greatest enhancement in rock reinforcement strength. In regions susceptible to slurry leakage, selecting a higher slurry volume ratio is advisable to expedite the sealing process and enhance the reinforcement strength of the rock.

Data availability

The data that support the findings of this study are available from the corresponding author upon reasonable request.

CRediT authorship contribution statement

Qing Ma: Methodology, Writing – original draft, Writing – review & editing. **Wei Zhang:** Funding acquisition, Methodology, Supervision, Writing – review & editing. **Xiaoli Liu:** Conceptualization, Funding acquisition, Supervision, Writing – review & editing. **Weiqiang Xie:** Conceptualization, Writing – review & editing, polish. **Ruosong Wang:** Writing – review & editing, Data acquisition. **Jinpeng Zhao:** Data acquisition.

Declaration of competing interest

The authors declare that they have no known competing financial interests or personal relationships that could have appeared to influence the work reported in this paper.

Acknowledgement

The research described in this paper was financially supported by the National Natural Science Foundation of China (Grant Nos. 52304136 and 52304093), China Post-

doctoral Science Foundation (Grant No. 2023M741968), and Key Project of Research and Development in Liaocheng City (Grant No. 2023YD02).

References

Afrasiabian, B., & Eftekhari, M. (2022). Prediction of mode I fracture toughness of rock using linear multiple regression and gene expression programming. *Journal of Rock Mechanics and Geotechnical Engineering, 14*(5), 1421–1432.

Agheshlui, H., Sedaghat, M. H., & Azizmohammadi, K. S. (2019). A comparative study of stress influence on fracture apertures in fragmented rocks. *Journal of Rock Mechanics and Geotechnical Engineering, 11*(1), 38–45.

Bai, C. H., Xue, Y. G., Qin, D. H., Su, M. X., Ma, X. M., & Liu, H. T. (2021). Analysis of factors affecting the deformation of soft rock tunnels by data envelopment analysis and a risk assessment model. *Tunnelling and Underground Space Technology, 116*, 104111.

Cai, X., Zhou, Z. L., Tan, L. H., Zang, H. Z., & Song, Z. T. (2020). Water saturation effects on thermal infrared radiation features of rock materials during deformation and fracturing. *Rock Mechanics and Rock Engineering, 53*(11), 4839–4856.

Cao, K. W., Ma, L. Q., Wu, Y., Khan, N. M., Spearing, A. J., Hussain, S., & Yang, J. (2021). Cyclic fatigue characteristics of rock failure using infrared radiation as precursor to violent failure: Experimental insights from loading and unloading response. *Fatigue & Fracture of Engineering Materials & Structures, 44*(2), 584–594.

Chen, D. H., Chen, H. E., Zhang, W., Lou, J. Q., & Bo, S. (2022). An analytical solution of equivalent elastic modulus considering confining stress and its variables sensitivity analysis for fractured rock masses. *Journal of Rock Mechanics and Geotechnical Engineering, 14*(3), 825–836.

Chen, F. Y., Wang, L., & Zhang, W. G. (2019). Reliability assessment on stability of tunnelling perpendicularly beneath an existing tunnel considering spatial variabilities of rock mass properties. *Tunnelling and Underground Space Technology, 88*, 276–289.

Dai, L. P., Zhao, X., Pan, Y. S., Luo, H., Gao, Y. N., Wang, A. W., Ding, L. L., & Li, P. (2025). Microseismic criterion for dynamic risk assessment and warning of roadway rockburst induced by coal mine seismicity. *Engineering Geology, 357*, 108324.

Feng, G. L., Chen, B. R., Xiao, Y. X., & Zhang, W. (2022). Microseismic characteristics of rockburst development in deep TBM tunnels with alternating soft-hard strata and application to rockburst warning: A case study of the Neelum-Jhelum hydropower project. *Tunnelling and Underground Space Technology, 122*, 104398.

Han, Z. Y., Li, D. Y., & Li, X. B. (2022). Dynamic mechanical properties and wave propagation of composite rock-mortar specimens based on SHPB tests. *International Journal of Mining Science and Technology, 32*(4), 793–806.

Hoang, N. Q., Kim, S. Y., & Lee, J. S. (2022). Compressibility, stiffness and electrical resistivity characteristics of sand-diatom mixtures. *Géotechnique, 72*(12), 1068–1081.

Hu, S. C., Zhang, C. X., & Ru, W. K. (2023). Creep properties and energy evolution characteristics of weakly cemented rock under step loading. *International Journal of Rock Mechanics and Mining Sciences, 170*, 105428.

Le, T., & Airey, D. (2023). Mechanical behaviour of a weakly structured soil at low confining stress. *Géotechnique, 73*(2), 128–142.

Li, G., Ma, F. S., Guo, J., Zhao, H. J., & Liu, G. (2020). Study on deformation failure mechanism and support technology of deep soft rock roadway. *Engineering Geology, 264*, 105262.

Liu, X. R., Han, Y. F., Li, D. L., Tu, Y. L., Deng, Z. Y., Yu, C. T., & Wu, X. C. (2019). Anti-pull mechanisms and weak interlayer parameter sensitivity analysis of tunnel-type anchorages in soft rock with underlying weak interlayers. *Engineering Geology, 253*, 123–136.

Ma, Q., Liu, X. L., Tan, Y. L., Wang, Y. R., Wang, R. S., Wang, E. Z., Liu, X. S., Zhao, Z. H., Ren, D. R., Xie, W. Q., Qian, R. P., & Hu, N. (2023). Monitoring and evaluation of disaster risk caused by linkage failure and instability of residual coal pillar and rock strata in multi-coal seam mining. *Geohazard Mechanics, 1*(4), 297–307.

Ma, Q., Tan, Y. L., Liu, X. S., Gu, Q. H., & Li, X. B. (2020). Effect of coal thicknesses on energy evolution characteristics of roof rock-coal-floor rock sandwich composite structure and its damage constitutive model. *Composites Part B-Engineering, 198*(1), 108086.

Ma, Q., Zhao, Z. H., Gao, X. J., Chen, S. J., & Tan, Y. L. (2019). Numerical survey on the destabilization mechanism of weakly cemented soft rock roadway considering interlayer effect. *Geotechnical and Geological engineering, 37*(11), 95–105.

Meng, N. K., Bai, J. B., & Chungsik, Y. (2023). Failure mechanism and control technology of deep soft-rock roadways: Numerical simulation and field study. *Underground Space, 12*, 1–17.

Mezza, S., Vazquez, P., Jemai, M. B., & Fronteau, G. (2022). Infrared thermography for the investigation of physical-chemical properties and thermal durability of Tunisian limestone rocks. *Construction and Building Materials, 339*, 127470.

Miao, S. Y., Cheng, G. W., Zhang, H. J., Huang, Y. Q., Gu, N., Zha, H. S., & Gao, J. (2023). Efficiently identifying coalbed methane enrichment areas by detecting and locating low-frequency signals in the coal mine. *Geohazard Mechanics, 1*(1), 86–93.

Mineo, S., & Pappalardo, G. (2019). InfraRed thermography presented as an innovative and non-destructive solution to quantify rock porosity in laboratory. *International Journal of Rock Mechanics and Mining Sciences, 115*, 99–110.

Mineo, S., Pappalardo, G., Casciano, C. I., Stefano, A. D., Catalano, S., & Gagliano, M. (2021). Insights on the Capo d'Orlando flysch (NE Sicily) by means of geomechanics and sedimentology. *Italian Journal of Geosciences, 138*(3), 404–417.

Ru, W. K., Hu, S. C., Zhou, A. H., Luo, P. K., Cong, H., Zhang, C. X., & Zhou, X. D. (2023). Study on creep characteristics and nonlinear fractional order damage constitutive model of weakly cemented soft rock. *Rock Mechanics Rock Engineering, 56*(11), 1–22.

Sivakumar, V., Moorhead, M. C., Donohue, S., Serridge, C., Tripathy, S., Mckinley, J., & Doherty, C. (2021). The initial, primary and secondary consolidation response of soft clay reinforced with a granular column under isolated loading. *Géotechnique, 71*(6), 467–479.

Swan, G., & Li, C. C. (2023). Hardrock burst mechanisms and management strategies. *Geohazard Mechanics, 1*(1), 18–31.

Tan, Z., Li, S., Yang, Y., & Wang, J. (2022). Large deformation characteristics and controlling measures of steeply inclined and layered soft rock of tunnels in plate suture zones. *Engineering Failure Analysis, 131*(5), 105831.

Tao, K., Dang, W. A., & Li, Y. C. (2023). Frictional sliding of infilled planar granite fracture under oscillating normal stress. *International Journal of Mining Science and Technology, 33*(6), 687–701.

Vazaios, I., Vlachopoulos, N., & Diederichs, M. S. (2019). Assessing fracturing mechanisms and evolution of excavation damaged zone of tunnels in interlocked rock masses at high stresses using a finite-discrete element approach. *Journal of Rock Mechanics and Geotechnical Engineering, 11*(4), 701–722.

Wang, G., Jiang, C., Shen, J., Han, D., & Qin, X. (2019). Deformation and water transport behaviors study of heterogenous coal using ct-based 3d simulation. *International Journal of Coal Geology, 211*, 103204.

Watanabe, Y., & Tanaka, Y. (2023). Swelling pressure of compacted bentonite acting on constraining material with deformability. *Géotechnique, 73*(2), 95–104.

Wei, M. D., Dai, F., Liu, Y., & Jiang, R. C. (2023). A fracture model for assessing tensile mode crack growth resistance of rocks. *Journal of Rock Mechanics and Geotechnical Engineering, 15*(2), 395–411.

Wu, Q., Liu, Y. X., Tang, H. M., Kang, J. T., Wang, L. Q., Li, C. D., Wang, D., & Liu, Z. Q. (2023). Experimental study of the influence of wetting and drying cycles on the strength of intact rock samples from a red stratum in the three Gorges Reservoir area. *Engineering Geology, 314*, 107013.

Xie, H. P., Lu, J., Li, M. H., & Gao, M. Z. (2022). Experimental study on the mechanical and failure behaviors of deep rock subjected to true triaxial stress: A review. *International Journal of Mining Science and Technology, 32*(5), 915–950.

Yang, S. Q., Chen, M., Fang, G., Wang, Y. C., Meng, B., Li, Y. G., & Jing, H. W. (2018). Physical experiment and numerical modelling of tunnel excavation in slanted upper-soft and lower-hard strata. *Tunnelling and Underground Space Technology, 82*, 248–264.

Yang, S. Q., Tao, Y., Xu, P., & Chen, M. (2019). Large-scale model experiment and numerical simulation on convergence deformation of tunnel excavating in composite strata. *Tunnelling and Underground Space Technology, 94*, 103133.

Zhang, C. Q., Cui, G. J., Deng, L., Zhou, H., Lu, J. J., & Dai, F. (2020a). Laboratory investigation on shear behaviors of bolt-grout interface subjected to constant normal stiffness. *Rock Mechanics and Rock Engineering, 53*, 1333–1347.

Zhang, W., Guo, W. Y., & Wang, Z. Q. (2022). Influence of lateral pressure on mechanical behavior of different rock types under biaxial compression. *Journal of Central South University, 29*(11), 3695–3705.

Zhang, W., Xing, M. L., & Guo, W. Y. (2023). Study on fracture characteristics of anchored sandstone with precast crack based on double K criterion. *International Journal of Solids and Structures, 275*, 112296.

Zhang, W. G., Somerville, I., Paneiro, G., Nong, X. Z., Chwala, M., & Yang, W. Y. (2024a). Design and construction of tunnels and tunneling: Understanding the importance of geological conditions, landslide susceptibility and risk assessment. *Geological Journal, 59*(9), 2365–2370.

Zhang, W. G., Tang, X. C., Yang, W. Y., Jiang, J. Q., Zhang, H. T., & Li, P. X. (2024b). Review of tunnels and tunneling in unfavorable geological conditions. *Geological Journal, 59*(9), 2668–2689.

Zhang, X. P., Lv, G. G., Liu, Q. S., Wu, S. C., Zhang, Q., Ji, P. Q., & Xu, H. T. (2020b). Identifying accurate crack initiation and propagation thresholds in siliceous siltstone and limestone. *Rock Mechanics and Rock Engineering, 52*(2), 1–8.

Zhang, Z. T., & Gao, W. H. (2020). Effect of different test methods on the disintegration behaviour of soft rock and the evolution model of disintegration breakage under cyclic wetting and drying. *Engineering Geology, 279*, 105888.

Zhao, J. P., Tan, Z. S., Wang, X. Y., Zhou, Z. L., & Li, G. L. (2021). Engineering characteristics of water-bearing weakly cemented sandstone and dewatering technology in tunnel excavation. *Tunnelling and Underground Space Technology, 121*, 104316.

Zhao, J. P., Tan, Z. S., Yu, R. S., Li, Z. L., & Wang, X. Y. (2022a). Mechanical responses of a shallow-buried super-large-section tunnel in weak surrounding rock: A case study in Guizhou. *Tunnelling and Underground Space Technology, 131*, 104850.

Zhao, J. P., Tan, Z. S., Zhang, B. J., & Wang, F. X. (2024). Stress release technology and engineering application of advanced center drifts in a super deep soft rock tunnel: A case study of the Haba Snow Mountain Tunnel. *Rock Mechanics and Rock Engineering, 57*(9), 7103–7124.

Zhao, S., Wu, S. L., Yang, L. L., & Wang, H. (2017). Analysis of secondary roof structure of the working face in Shendong mining area. *Geotechnical and Geological Engineering, 35*(1), 195–202.

Zhao, Z. H., Tan, Y. L., Chen, S. J., Ma, Q., & Gao, X. J. (2019). Theoretical analyses of stress field in surrounding rocks of weakly consolidated tunnel in a high-humidity deep environment. *International Journal of Rock Mechanics and Mining Sciences, 122*, 104064.